iScience

CellPress
OPEN ACCESS

Article

Optical clearing of living brains with MAGICAL to extend *in vivo* imaging

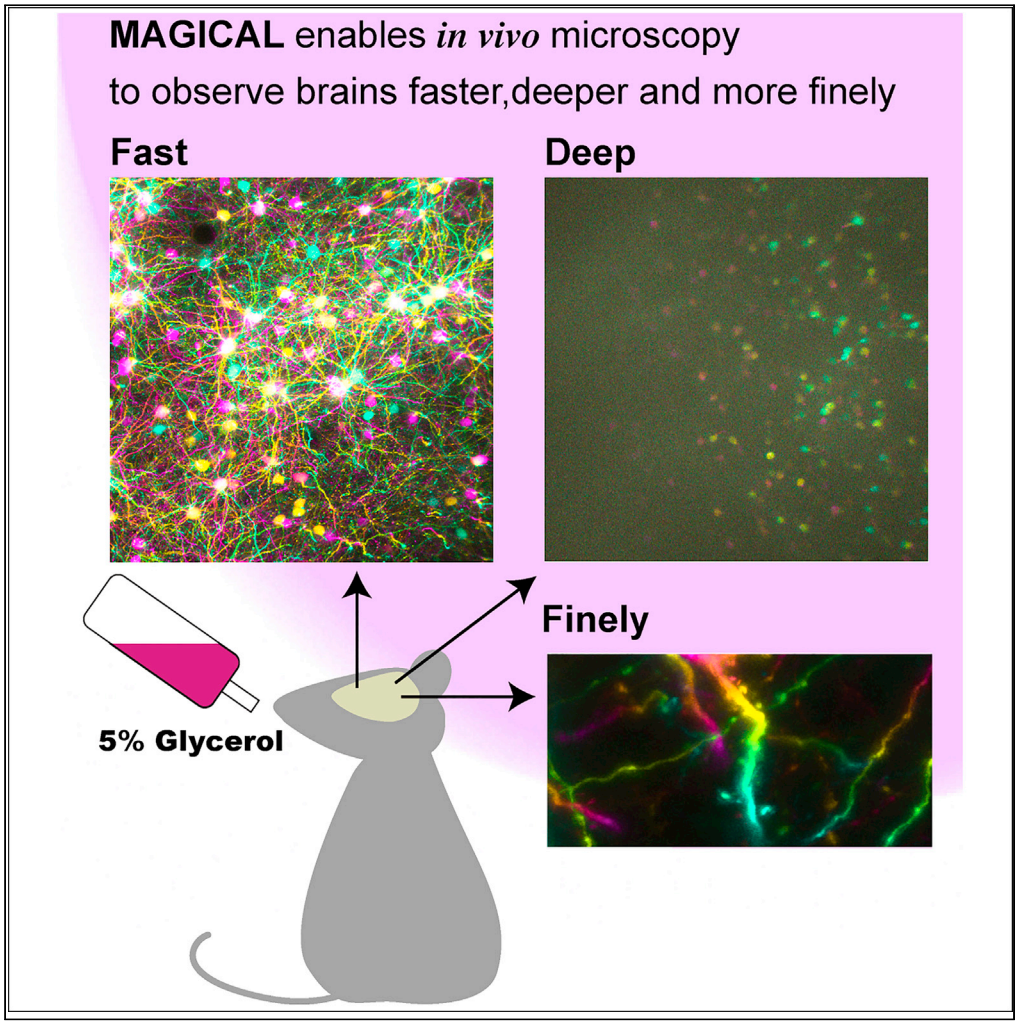

Kouichirou Iijima, Takuto Oshima, Ryosuke Kawakami, Tomomi Nemoto

tn@nips.ac.jp

HIGHLIGHTS

Oral glycerol administration (MAGICAL) enhances fluorescent signals in living brains

MAGICAL achieves *in vivo* optical clearing for living brains via scattering reduction

MAGICAL enables *in vivo* microscopy to observe brains faster, deeper, and more finely

Iijima et al., iScience *24*, 101888
January 22, 2021
https://doi.org/10.1016/j.isci.2020.101888

iScience

CellPress
OPEN ACCESS

Article

Optical clearing of living brains with MAGICAL to extend *in vivo* imaging

Kouichirou Iijima,[1] Takuto Oshima,[2] Ryosuke Kawakami,[1,2] and Tomomi Nemoto[1,2,3,4,5,6,*]

SUMMARY

To understand brain functions, it is important to observe directly how multiple neural circuits are performing in living brains. However, due to tissue opaqueness, observable depth and spatiotemporal resolution are severely degraded *in vivo*. Here, we propose an optical brain clearing method for *in vivo* fluorescence microscopy, termed MAGICAL (magical additive glycerol improves clear alive luminance). MAGICAL enabled two-photon microscopy to capture vivid images with fast speed, at cortical layer V and hippocampal CA1 *in vivo*. Moreover, MAGICAL promoted conventional confocal microscopy to visualize finer neuronal structures including synaptic boutons and spines in unprecedented deep regions, without intensive illumination leading to phototoxic effects. Fluorescence emission spectrum transmissive analysis showed that MAGICAL improved *in vivo* transmittance of shorter wavelength light, which is vulnerable to optical scattering, thus unsuited for *in vivo* microscopy. These results suggest that MAGICAL would transparentize living brains via scattering reduction.

INTRODUCTION

How do neurons work together for brain functions in living animals? In the brain, numerous neurons connect to each other three-dimensionally to form neural circuits underlying brain functions. Functional characteristics of neural circuits depend on neuronal activity and synaptic connectivity, both of which are reflected in fine sculptural distinctions in many cases (Chen et al., 2011; Matsuzaki et al., 2004; Trachtenberg et al., 2002). Multiple neural circuits are associated with each other as a neural network and are executed for rapid processing simultaneously to respond to various situations and their transitions (Margolis et al., 2012). Therefore, to understand brain functions, *in vivo* imaging techniques are required to observe intact neural circuits extended into deep regions, at high spatiotemporal resolution.

Confocal microscopy and two-photon microscopy can provide three-dimensional (3D) and time-lapse images by sequential optical sectioning in thick specimens without mechanical destruction (Ishikawa-Ankerhold et al., 2012; Nemoto, 2008). However, it is difficult for fluorescence microscopy, especially confocal microscopy, to achieve sufficiently deep, fine, and fast imaging *in vivo* because tissue opaqueness disturbs and attenuates both excitation lights and fluorescence signals. A simple but practical technique to overcome the opaqueness is high-intensity illumination by using a high-power excitation laser, but it has a risk of causing invasive phototoxic problems via reactive oxygen species production. Thus, new strategies are needed to overcome tissue opaqueness for *in vivo* imaging.

Recently, many optical clearing methods were reported for fluorescence microscopy in fixed organs including brains (Aoyagi et al., 2015; Chung et al., 2013; Ertürk et al., 2012; Hama et al., 2011; Ke et al., 2013; Kuwajima et al., 2013; Susaki et al., 2014). These clearing methods enable confocal microscopy to achieve fine and deeper imaging and have brought a paradigm shift in connectome analysis to create connection maps over comprehensive neural networks. However, these clearing methods need non-physiological procedures to transparentize fixed organs and thus are especially inapplicable to living brains for *in vivo* fluorescence microscopy. Here, we propose a new strategy for brain clearing in *in vivo* microscopy. Our clearing method is simply based on glycerol administration via drinking water, so we named it MAGICAL (magical additive glycerol improves clear alive luminance).

[1]Research Institute for Electronic Science, Hokkaido University, N20W10, Kita-ku, Sapporo, Hokkaido 001-0020, Japan

[2]Graduate School of Information Science and Technology, Hokkaido University, N14W9, Kita-ku, Sapporo, Hokkaido 060-0814, Japan

[3]Division of Biophotonics, National Institute for Physiological Sciences, National Institutes of Natural Sciences, Higashiyama 5-1, Myodaiji, Okazaki 444-0865, Aichi, Japan

[4]Biophotonics Research Group, Research Center on Life and Living Systems (ExCELLS), National Institutes of Natural Sciences, Higashiyama 5-1, Myodaiji, Okazaki, Aichi 444-8787, Japan

[5]School of Life Science, The Graduate University for Advanced Studies (SOKENDAI), Higashiyama 5-1, Myodaiji, Okazaki, Aichi 444-8787, Japan

[6]Lead Contact

*Correspondence: tn@nips.ac.jp

https://doi.org/10.1016/j.isci.2020.101888

RESULTS

Enhanced fluorescence signals *in vivo*

For *in vivo* brain imaging with fluorescence microscopy, the conventional method involves open-skull surgery. It consists of making a cranial window, in which the light-scattering skull bone is replaced by a clear cover glass, and is conceived as a key step affecting the quality of images in day-to-day experiments (Holtmaat et al., 2009). The cranial window and probably the brain itself lose transparency easily, which may be caused by unsuitable surgical techniques leading to bleeding and damage inside/outside the brain and by unknown factors related with the recovery process. Thus, a smaller cranial window is biologically preferred to avoid injuring blood vessels and to suppress changes of intracranial pressure at craniotomy and to minimize contact between the brain surface and the surgical materials (Holtmaat et al., 2009). However, a larger cranial window is optically preferred to collect even light emitted from a focal point at wide radiation angles, by using a high-numerical-aperture lens which governs spatial resolution and fluorescence intensity in imaging. Moreover, a panoramic window replacing most of the parietal bone is necessary for comprehensive imaging to observe the multi-brain area simultaneously.

To make the optically suited window but not to lose the transparency of the brain, a dogma indicated that researchers must master technical skills that achieve the open-skull surgery with much less contacting and invading to the brain. If the dogma is true, most open-skull surgeries indeed lose the transparency of living brains due to damage, especially in the comprehensive imaging. As a solution, we suppose that the optical clearing of living brains may be achieved by pharmacological approaches suppressing damage processes. We focused on glycerol oral administration, which is known to suppress cerebral edema in neurosurgical patients and suggested to supply energy to ischemic neurons in cerebral stroke (Berger et al., 2005; Cantore et al., 1964; Frank et al., 1981; Mathew et al., 1972; Meyer et al., 1971, 1975; Sloviter et al., 1966; Wald and McLaurin, 1982), because the edema is an early hallmark of damaged brains.

First, we examined whether oral administration of glycerol improves cerebral fluorescence images of *in vivo* two-photon microscopy. As MAGICAL, glycerol was added at 5% (w/v) concentration to drinking water for oral administration from 2 weeks prior to open-skull surgery to the end of the experiment except for the surgery and the observation. We performed *in vivo* imaging in acute stages of recovery after surgery. Because, from the following stages (a few days after surgery), fibrotic tissue often grows at a space between a cover glass and dura matter covering a brain, it thus makes the window opaque independent of the transparency of a living brain. To visualize neural circuits, we used adult H-line mice (Thy1-EYFP-H), which express enhanced yellow fluorescent protein (EYFP) in some of the pyramidal neurons. To avoid selection bias under uneven EYFP expression, the imaging area was selected according to the xy position where the hippocampus was observable at the most shallow depth. We captured 3D stacks as z series of xy images, using a two-photon microscope with 960-nm Ti:sapphire laser light. The xy images were acquired as 512 × 512 pixels at 1 frame per sec (fps), 2.2 μsec per pixel, which is the maximum speed in this condition.

The images of the cortical layer V (CxLV) neurons were captured with a 3-μm z-step size (Video S1) and were reconstructed with depth color-coded maximum intensity projection (DccMIP). In mice without glycerol administration (control), fluorescence images showed the pyramidal neuron cell bodies with basal dendrites, but the density was poor as a consequence of weak capture conditions (Figure 1A, Video S1). In contrast, in mice with 5% (w/v) glycerol administration (MAGICAL), bright fluorescence images showed many cell bodies and basal dendrites with high density (Figures 1A and Video S1).

In CxLV images at three different depths (Figure S1), fluorescence intensity distribution (FID) indicated that signals tended to increase with MAGICAL (Figure S2). However, it was not simple to summarize the FIDs for statistical analysis. The FIDs showed large individual differences within each treatment group, obscuring differences between the groups. Moreover, the FIDs had non-normal distributions extending beyond the detector's dynamic range. To overcome these problems, we evaluated fluorescence intensities of pixels (FIPs) in the image stacks, by using a generalized linear mixed model (GLMM). The FIPs were randomly selected from the stack and collected as samples, if not saturation or zero intensity, and were used as a response variable in the GLMM with a Gamma error distribution and a log link function. In the GLMM, "treatment" (MAGICAL or control) and "depth" (3 levels) were assigned as fixed effects, and "mouse" was assigned as a random effect for intercepts and "depth" slopes. The GLMM comprised 929,331 FIPs in 78 image stacks, extracted from 3 depths of 26 mice (n = 13 mice in each treatment) under 2 treatments ($R^2_{GLMM(m)}$: 0.0147, $R^2_{GLMM(c)}$: 0.200, Table S1A). In estimation for fixed effects, the GLMM

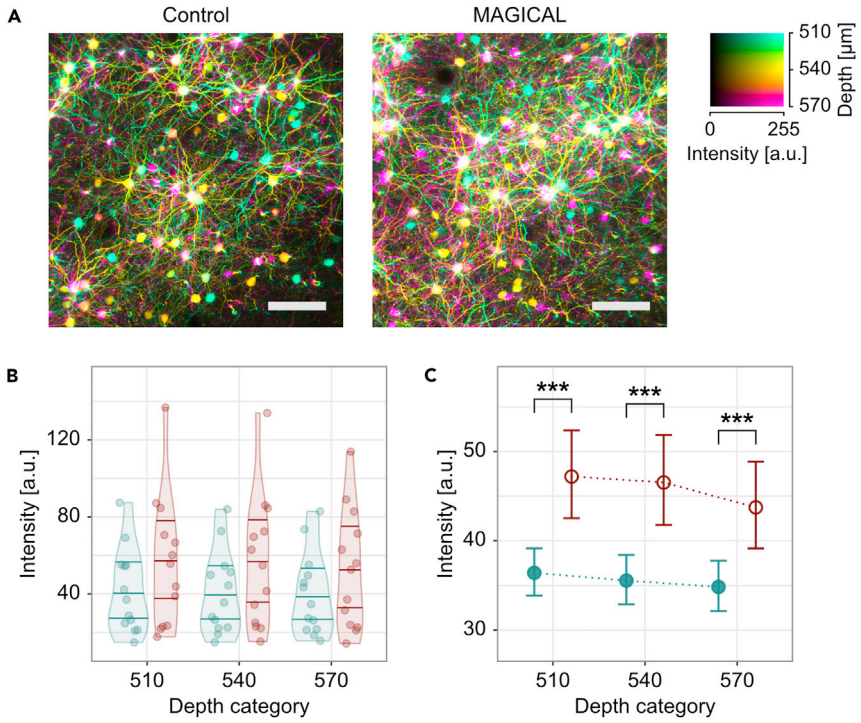

Figure 1. *In vivo* two-photon imaging at CxLV

(A) DccMIP images of CxLV at 540 ± 30 μm depth in control and MAGICAL. Scale bar represents 100 μm.

(B–C) Representative fluorescence intensity, predicted by the GLMM for each image stack (B) and "treatment" group (C), along "depth." The distribution of plots in (B) is visualized with violin plots estimated by Gaussian kernel and with 0.25, 0.50, and 0.75 quantile lines. Error bars in (C) are asymptotic 95% CI. Red, MAGICAL; blue, control; ***$p < 0.001$; a.u., arbitrary unit. See also Figures S1 and S2, Table S1, and Video S1.

indicated that MAGICAL enhanced FIPs in the CxLV images (Figures 1B and 1C; $p < 0.001$ at each "depth" level by pairwise comparison). These signal enhancements mean that MAGICAL can overcome tissue opaqueness enough to improve *in vivo* imaging.

In vivo two-photon deep imaging with fast speed

To achieve *in vivo* imaging in deeper regions, the most effective strategy is to use much longer wavelength, less scattered, near-infrared light at high power for two-photon excitation (Kawakami et al, 2013, 2015; Theer et al., 2003). Recently, hippocampal granule cells in the dentate gyrus were visualized at 1.5-mm depth in adult mice by using a 1064-nm laser diode light, in the most successful surgery without bleeding (Kawakami et al., 2015). Furthermore, hippocampal CA1 (HpCA1) neurons can be visualized at 1.0-mm depth in adult mice, by using 1000-nm Ti:sapphire laser light (Kawakami et al., 2015). However, despite the advantage of the longer wavelength strategy, fluorescence acquisitions must collect shorter visible light, attenuated more easily by scattering and absorption in tissues depending on return distance. Indeed, both deep imaging techniques require scanning neurons at 1/16 or fewer fps, which is extremely slow, to visualize neural activity and to overcome image distortions caused by heartbeats. So, as a touchstone of *in vivo* deep imaging, we examined whether MAGICAL improves adult HpCA1 images at fast scanning.

By using 960-nm Ti:sapphire laser light, HpCA1 images approximately at 1.0-mm depth were captured as 3D stacks, having xy images (512 × 512 pixels) with 1 fps fast speed. In control mice, fluorescence images showed some dim cell bodies of pyramidal neurons (Figures 2A and S3). In contrast, in MAGICAL mice, fluorescence images showed many cell bodies of pyramidal neurons, some of which were clearly visualized together with each apical dendrite descending into deeper regions (Figures 2A and S3).

In HpCA1 images captured from three different depths ±3 μm (Figure S4), FIDs were shifted to a bright side with MAGICAL (Figure S5). The GLMM at HpCA1 comprised 957,264 FIPs in 78 image stacks, extracted

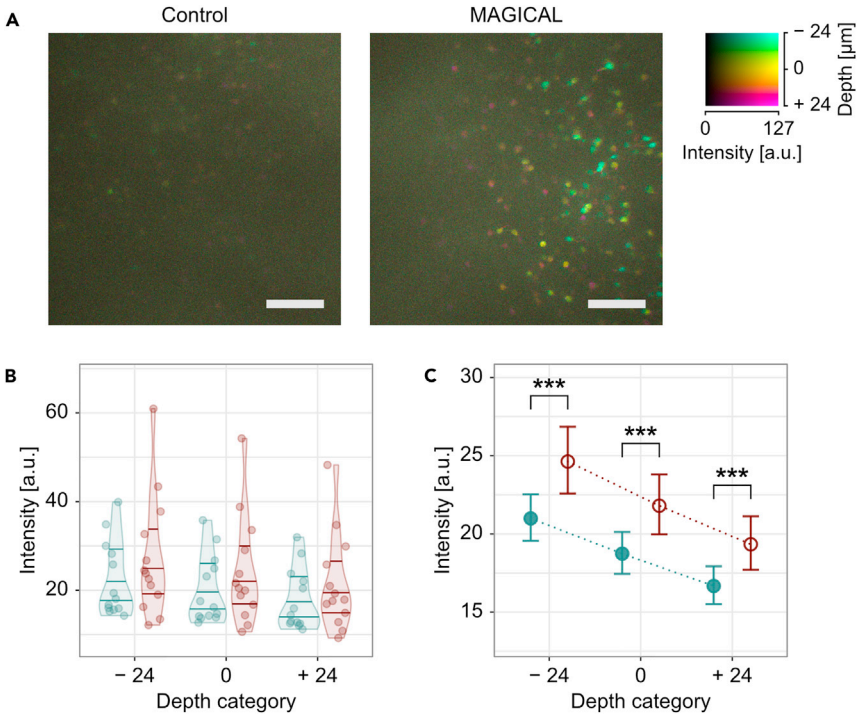

Figure 2. *In vivo* two-photon imaging at HpCA1

(A) DccMIP images of HpCA1 approximately at 975 ± 24 μm depth in control and MAGICAL. In the color code, each center depth is shown as 0 μm relative depth. Scale bar represents 100 μm.

(B–C) Representative fluorescence intensity, predicted by the GLMM for each image stack (B) and "treatment" group (C), along "depth." The distribution of plots in (B) is visualized with violin plots estimated by Gaussian kernel and with 0.25, 0.50, and 0.75 quantile lines. Error bars in (C) are asymptotic 95% CI. Red, MAGICAL; blue, control; ***p < 0.001; a.u., arbitrary unit. See also Figures S3, S4, S5, and Table S1.

from 3 depths of 26 mice (n = 13 mice in each treatment) under 2 treatments ($R^2_{GLMM(m)}$: 0.0714, $R^2_{GLMM(c)}$: 0.190, Table S1B). In estimation for fixed effects, the GLMM indicated that MAGICAL also enhanced FIPs in the HpCA1 images, despite long traversing from deep regions (Figures 2B and 2C; $p < 0.001$ at each "depth" level by pairwise comparison). These results suggest that MAGICAL would promote deep imaging as a practical method to visualize fast activity on mature neural circuits in adult mice.

In vivo confocal fine imaging with single-photon excitation in deeper regions

Despite its superior spatial resolution, confocal microscopy is less suitable for *in vivo* imaging than two-photon microscopy because its shorter wavelength excitation has an inferior penetration depth and a higher risk for phototoxic effects. Moreover, confocal microscopy cannot efficiently collect fluorescence signals due to a confocal aperture, which excludes most of the signals scattered by the tissue but is needed to remove extrafocal light causing image blur. Therefore, confocal microscopy is vulnerable to tissue opaqueness, especially optical scattering. In general, *in vivo* confocal microscopy is hardly able to visualize fine neural fibers below 50-μm depth, which poses a dilemma between clear visualization and phototoxicity reduction (Pérez-Alvarez et al., 2013). The above mentioned effects of MAGICAL on *in vivo* two-photon imaging suggest that it may overcome that dilemma.

Thus, we examined to what extent MAGICAL enables *in vivo* confocal microscopy to visualize neural fibers in deeper regions. We captured 3D stack images of cortical layer I (CxLI) at 50 ± 5, 100 ± 5, and 150 ± 5 μm depth in H-line mice, by using a confocal microscope with 488-nm laser light (CM image) and a two-photon microscope with 960-nm laser light (2PM image as a reference). The 3D stack images comprise a 1-μm-step z series of xy images, acquired as 512 × 512 pixels at 1 fps. In control mice, dim CM images at 100- and 150-μm depth were hardly able to visualize fine neural fibers except for thick shafts of apical dendrites which extend along the z axis direction (Figures 3A and S6). However, in MAGICAL mice, bright CM images

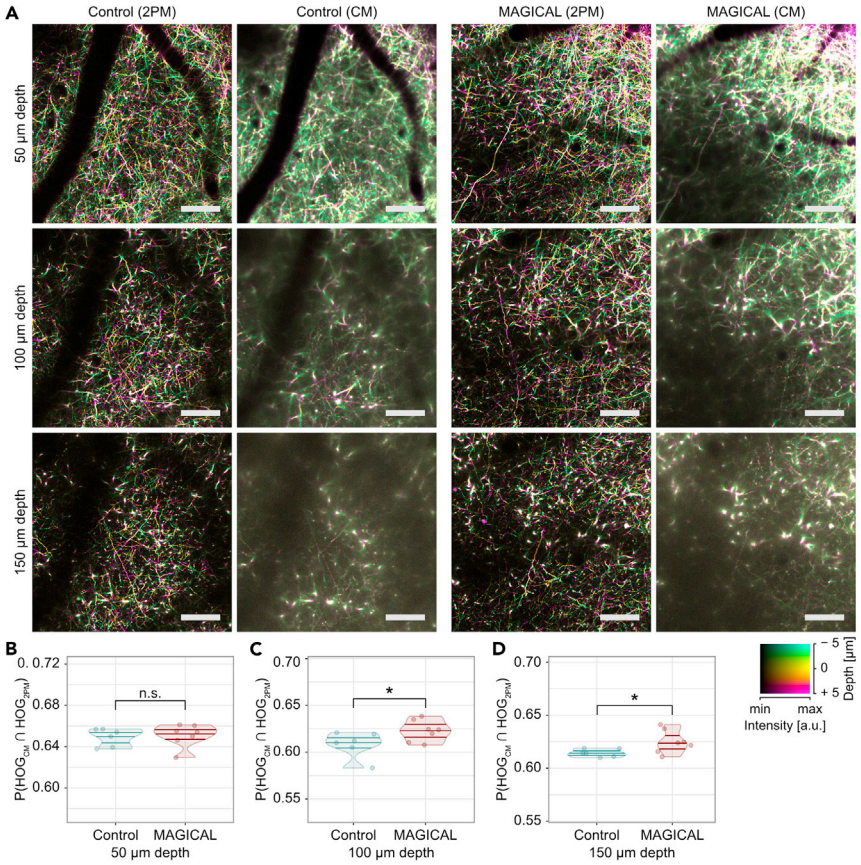

Figure 3. *In vivo* confocal imaging at CxLI

(A) DccMIP images of CxLI at 50 ± 5 μm, 100 ± 5 μm, and 150 ± 5 μm depth, by using two-photon microscopy (2PM) and confocal microscopy (CM). The display range of fluorescence intensity (min–max in 8 bits) is adjusted as follows: 2PM images at every depth, (0–127); CM images at 50, 100, and 150 μm depth, with (0–255), (0–127), and (0–63), respectively. In the color code, each center depth is shown as 0 μm relative depth. Scale bar represents 100 μm.

(B–D) Similarities of the DccMIP images between CM and 2PM at 50 ± 5 μm (B), 100 ± 5 μm (C), and 150 ± 5 μm (D) depth. $P(HOG_{CM} \cap HOG_{2PM})$, probability of intersection between HOG features extracted from the CM image and the 2PM image; $n = 6$ mice in control and $n = 7$ mice in MAGICAL; n.s., not significant; *$p < 0.05$; a.u., arbitrary unit. See also Figure S6.

even at 100- and 150-μm depth showed a lot of thin neuronal processes extending in the xy plane across the apical dendrite shaft (Figures 3A and S6).

We quantified similarities between CM images and 2PM reference images at the same CxLI areas, by using the intersection probability between histogram of oriented gradients (HOG) features extracted from each image. In the HOG comparison, CM images with MAGICAL retained more similarity to 2PM reference images at deeper regions (Figures 3B–3D, p = 0.0484 at 100 μm depth, p = 0.0420 at 150 μm depth, in permuted Brunner-Munzel test, $n = 6$ in control mice, $n = 7$ in MAGICAL mice). These results show that MAGICAL improves the observable depth at which *in vivo* confocal imaging can visualize detailed features.

To evaluate the visualization abilities of confocal microscopy with MAGICAL, we captured 3D stack images with high magnification at around 100-μm depth. In MAGICAL mice, the images showed synaptic structures, such as dendritic spines and axonal boutons, clearly, and fine fibers with less optical aberration along the z axis (Figures 4 and S7). Moreover, *in vivo* confocal images with MAGICAL did not show remarkable bleaching or phototoxic effects, as observed in time-lapse 3D stack imaging at 5-min intervals for 30 min (Figures 4 and S7). These data suggest that MAGICAL would provide a practical approach to observe deeper regions with superior spatial resolution beyond the dilemma posed by confocal microscopy.

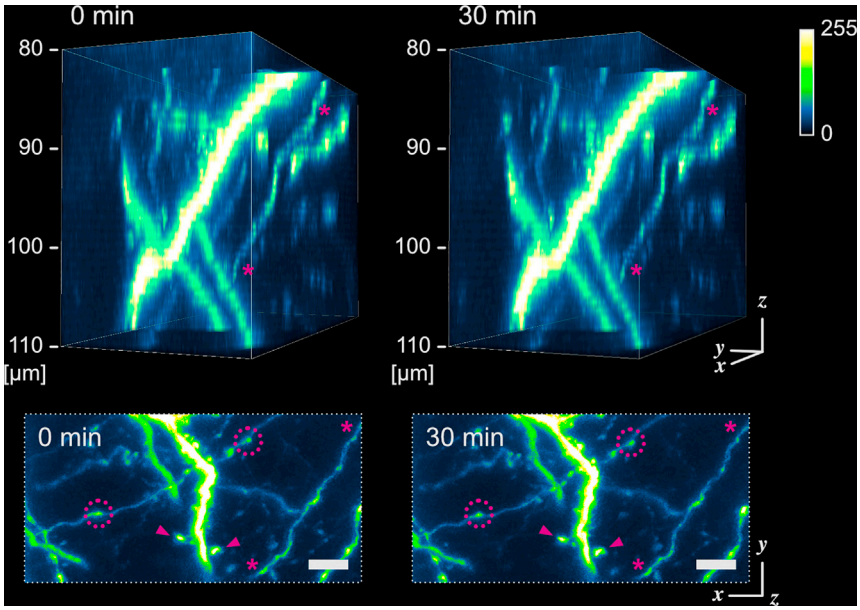

Figure 4. *In vivo* confocal high-resolution 4D imaging

Fine confocal 3D images with MAGICAL, captured with time lapse at 5-min intervals for 30 min. 3D images (upper) were reconstructed from 31 optical sections at 1 μm/step. A fine fiber (asterisk) was visualized with less optical aberration along the z axis under the appropriate setting of the confocal aperture. In maximum intensity projection (MIP) images (bottom), synaptic structures, such as dendritic spines (arrowhead) and axonal boutons (dotted circle), were observable. Despite a totality of 217 scans, remarkable bleaching and phototoxic effects were not observed. Scale bar represents 5 μm. See also Figure S7.

Evaluation of clearing ability by fluorescence emission spectrum transmissive analysis

Fluorescence signal enhancement at several depths is one of the phenomena expected with optical clearing. However, it remains unclear whether MAGICAL improves transparency inside living brains. To address the question, we tried to evaluate *in vivo* transmittance at different wavelengths through the brain.

In conventional transmissive analyses, a certified light source is needed on the other side of a detector beyond a target to calculate transmittance, i.e., the intensity ratio of transmissive light through a target to incident light from the source. In this perspective, fluorescence probes do not suit the light source for *in vivo* transmissive analysis because original fluorescence intensity within a focal point depends on the amount of the fluorescence probes and the intensity of transmitted excitation light, both of which are unknown and uncontrollable inside living brains. However, a fluorescence emission spectrum is physically certified as emission probability at wavelengths, determined by energy levels and transition frequencies inherent in its molecule. Thus, to evaluate *in vivo* transmittance, we developed a new analytical method, fluorescence emission spectrum transmissive analysis (FESTA), by using the emission spectrum as a scale-independence of whole fluorescence intensity.

As fluorescence resources of *in vivo* FESTA, artificial yellow-green (YG) beads (Fluoresbrite YG Microspheres, Calibration Grade 1 μm; Polysciences) were injected into living mouse brains and then were scattered in small clusters with cerebrospinal fluid flow. We calculated the spectral intensity ratio of cyan (458–511 nm) to yellow (560–650 nm) light within *in vivo* images of the bead clusters (Figure 5A). In contrast to fluorescence intensity, the cyan/yellow ratio was independent of both of amount of the fluorescence probes and two-photon excitation power (Figure S8). However, the cyan/yellow ratio was different between depths (Figure S8). Therefore, it is considered that the cyan/yellow ratio is proportional to a ratio, comprising the emission probability (constant), detector sensitivity (fixed as constant), and transmittance in the return path from inside the brain, for the cyan and yellow light.

To focus on internal transmittance in living brains and to remove the constant factors, we evaluated spectral transmission ratio (Δcyan/yellow) while the light returned from deeper regions to 100-μm depth. The

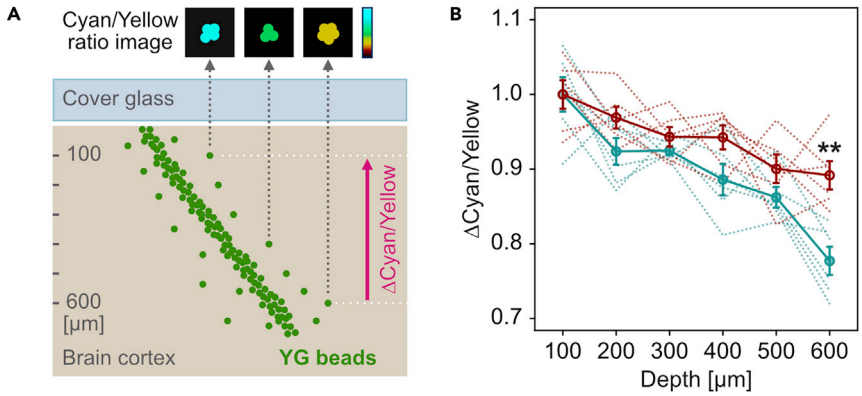

Figure 5. Optical evaluation for living brains

(A) Schematic illustration of the FESTA by using fluorescent YG bead clusters injected into living brains.

(B) *In vivo* spectral transmission ratio (Δcyan/yellow) while the light returned from deeper regions to 100-μm depth. Red, MAGICAL; blue, control; solid line, average with standard error; dotted line, each trial; $n = 6$ mice in each group; **$p < 0.01$. See also Figure S8.

Δcyan/yellow gradually decreased along with the depth (Figure 5B). It is, therefore, reasonable to consider that the cyan transmittance is more likely to be decreased than the yellow one because shorter wavelength light is more scattered depending on the optical path length. However, in MAGICAL, a decrease of Δcyan/yellow was suppressed at deeper regions ($p = 0.00159$ in unpaired two-tailed Welch's t test, 95% confidence interval [CI] = 0.0551–0.174, $t = 4.29$, $df = 10.0$, Cohen's $d = 2.48$, $n = 6$ mice in each group, at 600-μm depth). These results suggest that MAGICAL improves *in vivo* transmittance especially of shorter wavelength light susceptible to optical scattering. Thus, we conclude that MAGICAL exerts an optical clearing ability to reduce scattering in living brains.

DISCUSSION

MAGICAL improved clear fluorescence signals, which would be enough to achieve faster imaging in deeper regions *in vivo*. The imaging speed is one of the most important factors for *in vivo* observation. Fast imaging enables the visualization of not only instantaneous changes in neural activity with high temporal resolution but also finer structures of neural circuits by overcoming heartbeat-related trembles. In addition, fast imaging is required for enhancement of spatial resolution per time unit and expansion of observable areas within limited experimental time. Furthermore, fast imaging would be preferred to reduce phototoxic effects *in vivo*. Thus, MAGICAL would be a fundamental method for *in vivo* imaging to observe extensive neural circuits at high spatiotemporal resolution with less invasiveness.

Our results suggested that MAGICAL can transparentize living brains via scattering reduction. How does MAGICAL suppress the optical scattering in living brains? Generally, the major source of optical scattering in tissues is refractive index mismatches between structural components (n_d; approx. 1.5) and interstitial fluids (water, n_d; 1.33). A conventional optical clearing is achieved by increasing the refractive index of fluids with high index reagents that can infiltrate into tissues and/or replace original fluids with the reagents themselves and, as a result, reduce the mismatches (Gómez-Gaviro et al., 2020). Glycerol (n_d; 1.47 at 100%) is one of the major reagents for optical clearing. The conventional clearing approach is useful for *in vivo* imaging to observe inside/beyond tough tissues, such as the skin (Novoselova et al., 2020; Wen et al., 2010) and skull (Zhao et al., 2018), which tolerate glycerol immersion even at high concentration keeping a high refractive index. However, glycerol also causes hemolysis *in vivo* as a function of dose, concentration, and route of administration (Cameron and Finckh, 1956; Frank et al., 1981), indicating that the conventional technique using higher concentration glycerol is less applicable for almost *in vivo* tissues. In contrast, Iodixanol can achieve to increase the refractive index of medium without toxicity for soft living specimens; thus, it provides optical clearing for *in vivo* microscopy (Boothe et al., 2017). However, the optical clearing by iodixanol only occurs on the boundary between medium and specimens. Namely, iodixanol can reduce spherical aberrations caused on the surfaces of specimens but not transparentize specimens via scattering reduction. As long as the scattering reduction depends on the replacement of fluids, optical clearing inside soft living specimens would be impossible.

Importantly, MAGICAL achieves optical clearing of living brains regardless of low concentration glycerol (5%), which has almost the same refractive index as water. Some research studies suggested that physiological condition affects optical properties in living tissues via slight changes in solute concentration. In the glucose tolerance test performed on human subjects, a spectrometer detects that the reduced scattering coefficient in the muscle decreases during blood glucose level elevation (Maier et al., 1994). Optical coherence tomography (OCT) monitoring to skins (dermis) shows that signal decay according to observation depth is mitigated after blood glucose level elevation (Larin et al., 2002, 2003, 2012). These results suggest that glucose at the physiological concentration can reduce tissue scattering. However, OCT also shows that optical clearing occurs only at a lower dermis rich with microvessels but not at other outer layers in the skin (Larin et al., 2002). Therefore, the optical clearing with blood glucose level elevation would be insufficient for *in vivo* microscopy to improve image formation. Microscopy must make a focal point and thus cannot image clearly beyond scattering matter in the optical path. Indeed, any reagents, including glucose, have not yet provided optical clearing agents workable for microscopy even at low concentrations, except for glycerol in MAGICAL. Unlike glucose, glycerol passively permeates into cells through cell membranes and thus may contribute to clearing throughout living brains.

At least, it is clear that MAGICAL needs *in vivo* physiological reactions to provide optical clearing ability. As originally planned, we suppose that MAGICAL is a pharmacological approach rather than conventionally simple replacements and thus works even at a low concentration with less influence on index mismatch reduction. MAGICAL was designed in reference to the medical treatment for cerebral edema and ischemic stroke (Berger et al., 2005; Cantore et al., 1964; Frank et al., 1981; Mathew et al., 1972; Meyer et al., 1971, 1975; Wald and McLaurin, 1982). Cerebral edema may occur for various reasons: cerebral trauma and inflammation allow the leak of serum proteins, drawing fluid into the brain due to the breakdown of the blood-brain barrier (Kimelberg, 1995). Furthermore, ischemia and hypoxia cause cell swelling due to a dysfunction of ion pumps caused by energy depletion (Kimelberg, 1995). The cerebral edema, in turn, reduces blood flow (ischemia) as a consequence of intracranial hypertension, thereby deteriorating hypoxia. Clinically, glycerol is commonly administrated to patients undergoing neurosurgery and patients with stroke in order to reduce edema via dehydration, thus to decrease intracranial pressure (ICP) and to increase cerebral blood flow (Berger et al., 2005; Cantore et al., 1964; Meyer et al., 1971, 1975; Wald and McLaurin, 1982). From an optical point of view, light scattering is increased in living brains under cerebral ischemia and hypoxia, experimentally induced by blood removal and nitrogen gas inhalation, respectively (Kawauchi et al., 2008, 2011). The increased scattering is attributed to disturbances in cellular/subcellular structures due to energy depletion. In the case of *in vivo* microscopy, living brains are exposed to loads, such as open-skull surgery, illumination for fluorescence excitation, and slight hypoxia from anesthesia. These loads cause brain trauma and inflammation, which in turn would trigger local edema, which, although not as severe as experimental ischemia and hypoxia, is enough to increase scattering for shorter wavelength light. Altogether MAGICAL protects the living brains from edema and ischemia, it thus would preserve brain transparency.

What are the adverse effects of using MAGICAL for *in vivo* imaging? In toxicity tests, chronic oral glycerol has been shown as safe for animals, when administered in dosages equal to or lower than 9 g/kg-bw/day (Hine et al., 1953; Johnson et al., 1933). Thus, MAGICAL is considered as a non-invasive treatment, considering that 4.5-mL of 5% (w/v) glycerol is daily administered as drinking water to a mouse weighing approximately 25 g. In the treatment of cerebral edema, glycerol administration does not show severe ICP rebound, electrolyte imbalance, and toxic side effects (Berger et al., 2005; Cantore et al., 1964; Meyer et al., 1971; Wald and McLaurin, 1982). In addition, glycerol administration is expected to improve electroencephalogram and neurological status in patients with ischemic stroke (Mathew et al., 1972; Meyer et al., 1971, 1975). Moreover, glycerol administration is also commonly used to reduce intraocular pressure in patients with glaucoma, without significant side effects suggestive of neurologic dysfunction (Awasthi and Srivastava, 1965). These results suggest that MAGICAL would less disturb fundamental mechanisms executing brain functions. However, glycerol administration would improve energy metabolism in ischemic brains (Meyer et al., 1975), indicating that glycerol can be a cue to trigger some neural activity. The extent to which MAGICAL can modulate neural activity remains unclear and thus probably should be evaluated for each neural circuit of interest.

MAGICAL is the first candidate for the optical clearing method applicable to living brains, easily improving *in vivo* microscopy without requiring any special skills or devices. Improved transparency for shorter

wavelength light with MAGICAL means to expand the usability of various light sources, luminous probes, photosensitive caged compounds, and optogenetic tools for *in vivo* imaging and optical manipulation. In other words, MAGICAL is an important contribution toward scientific advance, requiring a multi-laser/probe combination, such as the stimulated emission depletion microscopy (Klar et al., 2000), photo-stimulation techniques (Noguchi et al., 2011), and multi-color imaging (Livet et al., 2007). Moreover, MAGICAL enables *in vivo* microscopy via the cranial window to be combined with other neurological methods that insert electrodes or glass capillaries. These classical methods have been less compatible with *in vivo* microscopy due to an open-skull dogma that prohibits from contacting the brain to capture clear images. However, FESTA demonstrated that MAGICAL has optical clearing ability on living brains by artificial beads injected by glass capillaries. Thus, MAGICAL would accelerate functional analysis for brain functions, only by oral administration of glycerol.

Limitations of the study

We did not examine the optical clearing ability of MAGICAL for chronic imaging. As aforementioned, the cranial window tends to be opaque in the recovery process for such reasons: bleeding and making fibrotic tissue on the dura. These opaque materials would occur a few days after surgery but partly or nearly completely disappear for 2–3 weeks. Optical transparency directly below the chronic cranial window is spatiotemporally various within recovered mice. Therefore, it is difficult to evaluate quantitatively how long and how extent MAGICAL achieves optical clearing in living brains for chronic imaging. However, considering that brains cannot fully recover from a stroke, we expect that the prevention of edema during the recovery process also contributes to the transparency of living brains for chronic imaging.

Resource availability

Lead contact

Further information and requests for resources and reagents should be directed to and will be fulfilled by the Lead Contact, Tomomi Nemoto (tn@nips.ac.jp).

Materials availability

This study did not generate new unique reagents.

Data and code availability

Data and code are available from the corresponding author upon request.

METHODS

All methods can be found in the accompanying Transparent Methods supplemental file.

SUPPLEMENTAL INFORMATION

Supplemental Information can be found online at https://doi.org/10.1016/j.isci.2020.101888.

ACKNOWLEDGMENTS

We thank Nikon Imaging Center (NIC) at Hokkaido University for technical support with a 60× objective lens. This research was supported by the "Brain/MIND" from the Japan Agency for Medical Research and Development (AMED) 20dm0207078; by the MEXT/JSPS KAKENHI Grant Number JP15H05953 "Resonance Bio", JP20H00523 and JP20H05669 from the Japan Society for the Promotion of Sciences (JSPS) in the Ministry of Education, Culture, Sports, Science and Technology (MEXT); by the "Network Joint Research Center for Materials and Devices" in the MEXT; and by the "Dynamic Alliance for Open Innovation Bridging Human, Environment and Materials" in the MEXT.

AUTHOR CONTRIBUTIONS

Conceptualization, K.I., R.K., and T.N.; Data Curation, K.I. and T.O.; Formal Analysis, K.I.; Funding Acquisition, T.N.; Investigation, K.I. and T.O.; Methodology, K.I.; Project Administration, K.I.; Resources, T.N.; Software, K.I.; Supervision, T.N.; Validation, K.I. and T.O.; Visualization, K.I.; Writing – Original Draft Preparation, K.I. and T.N.; Writing – Review & Editing, K.I. and T.N.

DECLARATION OF INTERESTS

The authors declare no conflicts of interest related to this research.

Received: June 9, 2020
Revised: October 2, 2020
Accepted: November 26, 2020
Published: January 22, 2021

REFERENCES

Aoyagi, Y., Kawakami, R., Osanai, H., Hibi, T., and Nemoto, T. (2015). A rapid optical clearing protocol using 2,2′-thiodiethanol for microscopic observation of fixed mouse brain. PLoS One *10*, e0116280.

Awasthi, P., and Srivastava, S.N. (1965). Role of oral glycerol in glaucoma. Br. J. Ophthalmol. *49*, 660–666.

Berger, C., Sakowitz, O.W., Kiening, K.L., and Schwab, S. (2005). Neurochemical monitoring of glycerol therapy in patients with ischemic brain edema. Stroke *36*, e4–e6.

Boothe, T., Hilbert, L., Heide, M., Berninger, L., Huttner, W.B., Zaburdaev, V., Vastenhouw, N.L., Myers, E.W., Drechsel, D.N., and Rink, J.C. (2017). A tunable refractive index matching medium for live imaging cells, tissues and model organisms. eLife *6*, e27240.

Cameron, G.R., and Finckh, E.S. (1956). The production of an acute haemolytic crisis by the subcutaneous injection of glycerol. J. Pathol. Bacteriol. *71*, 165–172.

Cantore, G., Guidetti, B., and Virno, M. (1964). Oral glycerol for the reduction of intracranial pressure. J. Neurosurg. *21*, 278–283.

Chen, X., Leischner, U., Rochefort, N.L., Nelken, I., and Konnerth, A. (2011). Functional mapping of single spines in cortical neurons *in vivo*. Nature *475*, 501–505.

Chung, K., Wallace, J., Kim, S.-Y., Kalyanasundaram, S., Andalman, A.S., Davidson, T.J., Mirzabekov, J.J., Zalocusky, K.A., Mattis, J., Denisin, A.K., et al. (2013). Structural and molecular interrogation of intact biological systems. Nature *497*, 332–337.

Ertürk, A., Becker, K., Jährling, N., Mauch, C.P., Hojer, C.D., Egen, J.G., Hellal, F., Bradke, F., Sheng, M., and Dodt, H.-U. (2012). Three-dimensional imaging of solvent-cleared organs using 3DISCO. Nat. Protoc. *7*, 1983–1995.

Frank, M.S.B., Nahata, M.C., and Hilty, M.D. (1981). Glycerol: a review of its pharmacology, pharmacokinetics, adverse reactions, and clinical use. Pharmacotherapy *1*, 147–160.

Gómez-Gaviro, M.V., Sanderson, D., Ripoll, J., and Desco, M. (2020). Biomedical applications of tissue clearing and three-dimensional imaging in health and disease. iScience *23*, 101432.

Hama, H., Kurokawa, H., Kawano, H., Ando, R., Shimogori, T., Noda, H., Fukami, K., Sakaue-Sawano, A., and Miyawaki, A. (2011). Sca*l*e: a chemical approach for fluorescence imaging and reconstruction of transparent mouse brain. Nat. Neurosci. *14*, 1481–1488.

Hine, C.H., Anderson, H.H., Moon, H.D., Dunlap, M.K., and Morse, M.S. (1953). Comparative toxicity of synthetic and natural glycerin. A.M.A. Arch. Ind. Hyg. Occup. Med. *7*, 282–291.

Holtmaat, A., Bonhoeffer, T., Chow, D.K., Chuckowree, J., De Paola, V., Hofer, S.B., Hübener, M., Keck, T., Knott, G., Lee, W.-C.A., et al. (2009). Long-term, high-resolution imaging in the mouse neocortex through a chronic cranial window. Nat. Protoc. *4*, 1128–1144.

Ishikawa-Ankerhold, H.C., Ankerhold, R., and Drummen, G.P.C. (2012). Advanced fluorescence microscopy techniques—FRAP, FLIP, FLAP, FRET and FLIM. Molecules *17*, 4047–4132.

Johnson, V., Carlson, A.J., and Johnson, A. (1933). Studies on the physiological action of glycerol on the animal organism. Am. J. Phys. *103*, 517–534.

Kawakami, R., Sawada, K., Kusama, Y., Fang, Y.-C., Kanazawa, S., Kozawa, Y., Sato, S., Yokoyama, H., and Nemoto, T. (2015). *In vivo* two-photon imaging of mouse hippocampal neurons in dentate gyrus using a light source based on a high-peak power gain-switched laser diode. Biomed. Opt. Express *6*, 891–901.

Kawakami, R., Sawada, K., Sato, A., Hibi, T., Kozawa, Y., Sato, S., Yokoyama, H., and Nemoto, T. (2013). Visualizing hippocampal neurons with *in vivo* two-photon microscopy using a 1030 nm picosecond pulse laser. Sci. Rep. *3*, 1014.

Kawauchi, S., Sato, S., Ooigawa, H., Nawashiro, H., Ishihara, M., and Kikuchi, M. (2008). Simultaneous measurement of changes in light absorption due to the reduction of cytochrome c oxidase and light scattering in rat brains during loss of tissue viability. Appl. Opt. *47*, 4164–4176.

Kawauchi, S., Sato, S., Uozumi, Y., Nawashiro, H., Ishihara, M., and Kikuchi, M. (2011). Light-scattering signal may indicate critical time zone to rescue brain tissue after hypoxia. J. Biomed. Opt. *16*, 027002.

Ke, M.-T., Fujimoto, S., and Imai, T. (2013). SeeDB: a simple and morphology-preserving optical clearing agent for neuronal circuit reconstruction. Nat. Neurosci. *16*, 1154–1161.

Kimelberg, H.K. (1995). Current concepts of brain edema - review of laboratory investigations. J. Neurosurg. *83*, 1051–1059.

Klar, T.A., Jakobs, S., Dyba, M., Egner, A., and Hell, S.W. (2000). Fluorescence microscopy with diffraction resolution barrier broken by stimulated emission. Proc. Natl. Acad. Sci. U S A *97*, 8206–8210.

Kuwajima, T., Sitko, A.A., Bhansali, P., Jurgens, C., Guido, W., and Mason, C. (2013). *Clear*^{T}: a detergent- and solvent-free clearing method for neuronal and non-neuronal tissue. Development *140*, 1364–1368.

Larin, K.V., Eledrisi, M.S., Motamedi, M., and Esenaliev, R.O. (2002). Noninvasive blood glucose monitoring with optical coherence tomography: a pilot study in human subjects. Diabetes Care *25*, 2263–2267.

Larin, K.V., Ghosn, M.G., Bashkatov, A.N., Genina, E.A., Trunina, N.A., and Tuchin, V.V. (2012). Optical clearing for OCT image enhancement and in-depth monitoring of molecular diffusion. IEEE J. Select. Top. Quan. Electron. *18*, 1244–1259.

Larin, K.V., Motamedi, M., Ashitkov, T.V., and Esenaliev, R.O. (2003). Specificity of noninvasive blood glucose sensing using optical coherence tomography technique: a pilot study. Phys. Med. Biol. *48*, 1371–1390.

Livet, J., Weissman, T.A., Kang, H., Draft, R.W., Lu, J., Bennis, R.A., Sanes, J.R., and Lichtman, J.W. (2007). Transgenic strategies for combinatorial expression of fluorescent proteins in the nervous system. Nature *450*, 56–62.

Maier, J.S., Walker, S.A., Fantini, S., Franceschini, M.A., and Gratton, E. (1994). Possible correlation between blood glucose concentration and the reduced scattering coefficient of tissues in the near infrared. Opt. Lett. *19*, 2062–2064.

Margolis, D.J., Lütcke, H., Schulz, K., Haiss, F., Weber, B., Kügler, S., Hasan, M.T., and Helmchen, F. (2012). Reorganization of cortical population activity imaged throughout long-term sensory deprivation. Nat. Neurosci. *15*, 1539–1546.

Mathew, N.T., Rivera, V.M., Meyer, J.S., Charney, J.Z., and Hartmann, A. (1972). Double-blind evaluation of glycerol therapy in acute cerebral infarction. Lancet *300*, 1327–1329.

Matsuzaki, M., Honkura, N., Ellis-Davies, G.C.R., and Kasai, H. (2004). Structural basis of long-term potentiation in single dendritic spines. Nature *429*, 761–766.

Meyer, J.S., Charney, J.Z., Rivera, V.M., and Mathew, N.T. (1971). Treatment with glycerol of cerebral œdema due to acute cerebral infarction. Lancet *298*, 993–997.

Meyer, J.S., Itoh, Y., Okamoto, S., Welch, K.M., Mathew, N.T., Ott, E.O., Sakaki, S., Miyakawa, Y., Chabi, E., and Ericsson, A.D. (1975). Circulatory and metabolic effects of glycerol infusion in patients with recent cerebral infarction. Circulation *51*, 701–712.

Nemoto, T. (2008). Living cell functions and morphology revealed by two-photon microscopy in intact neural and secretory organs. Mol. Cells *26*, 113–120.

Noguchi, J., Nagaoka, A., Watanabe, S., Ellis-Davies, G.C.R., Kitamura, K., Kano, M., Matsuzaki, M., and Kasai, H. (2011). *In vivo* two-photon uncaging of glutamate revealing the structure-function relationships of dendritic spines in the neocortex of adult mice. J. Physiol. (Lond.) *589*, 2447–2457.

Novoselova, M.V., Abakumova, T.O., Khlebtsov, B.N., Zatsepin, T.S., Lazareva, E.N., Tuchin, V.V., Zharov, V.P., Gorin, D.A., and Galanzha, E.I. (2020). Optical clearing for photoacoustic lympho- and angiography beyond conventional depth limit *in vivo*. Photoacoustics *20*, 100186.

Pérez-Alvarez, A., Araque, A., and Martin, E.D. (2013). Confocal microscopy for astrocyte *in vivo* imaging: recycle and reuse in microscopy. Front. Cell. Neurosci. *7*, 51.

Sloviter, H.A., Shimkin, P., and Suhara, K. (1966). Glycerol as a substrate for brain metabolism. Nature *210*, 1334–1336.

Susaki, E.A., Tainaka, K., Perrin, D., Kishino, F., Tawara, T., Watanabe, T.M., Yokoyama, C., Onoe, H., Eguchi, M., Yamaguchi, S., et al. (2014). Whole-brain imaging with single-cell resolution using chemical cocktails and computational analysis. Cell *157*, 726–739.

Theer, P., Hasan, M.T., and Denk, W. (2003). Two-photon imaging to a depth of 1000 μm in living brains by use of a Ti:Al_2O_3 regenerative amplifier. Opt. Lett. *28*, 1022–1024.

Trachtenberg, J.T., Chen, B.E., Knott, G.W., Feng, G., Sanes, J.R., Welker, E., and Svoboda, K. (2002). Long-term *in vivo* imaging of experience-dependent synaptic plasticity in adult cortex. Nature *420*, 788–794.

Wald, S.L., and McLaurin, R.L. (1982). Oral glycerol for the treatment of traumatic intracranial hypertension. J. Neurosurg. *56*, 323–331.

Wen, X., Mao, Z., Han, Z., Tuchin, V.V., and Zhu, D. (2010). *In vivo* skin optical clearing by glycerol solutions: mechanism. J. Biophotonics *3*, 44–52.

Zhao, Y.-J., Yu, T.-T., Zhang, C., Li, Z., Luo, Q.-M., Xu, T.-H., and Zhu, D. (2018). Skull optical clearing window for *in vivo* imaging of the mouse cortex at synaptic resolution. Light Sci. Appl. *7*, 17153.

iScience, Volume *24*

Supplemental Information

Optical clearing of living brains with MAGICAL to extend *in vivo* imaging

Kouichirou Iijima, Takuto Oshima, Ryosuke Kawakami, and Tomomi Nemoto

Supplemental Figures and Legends:

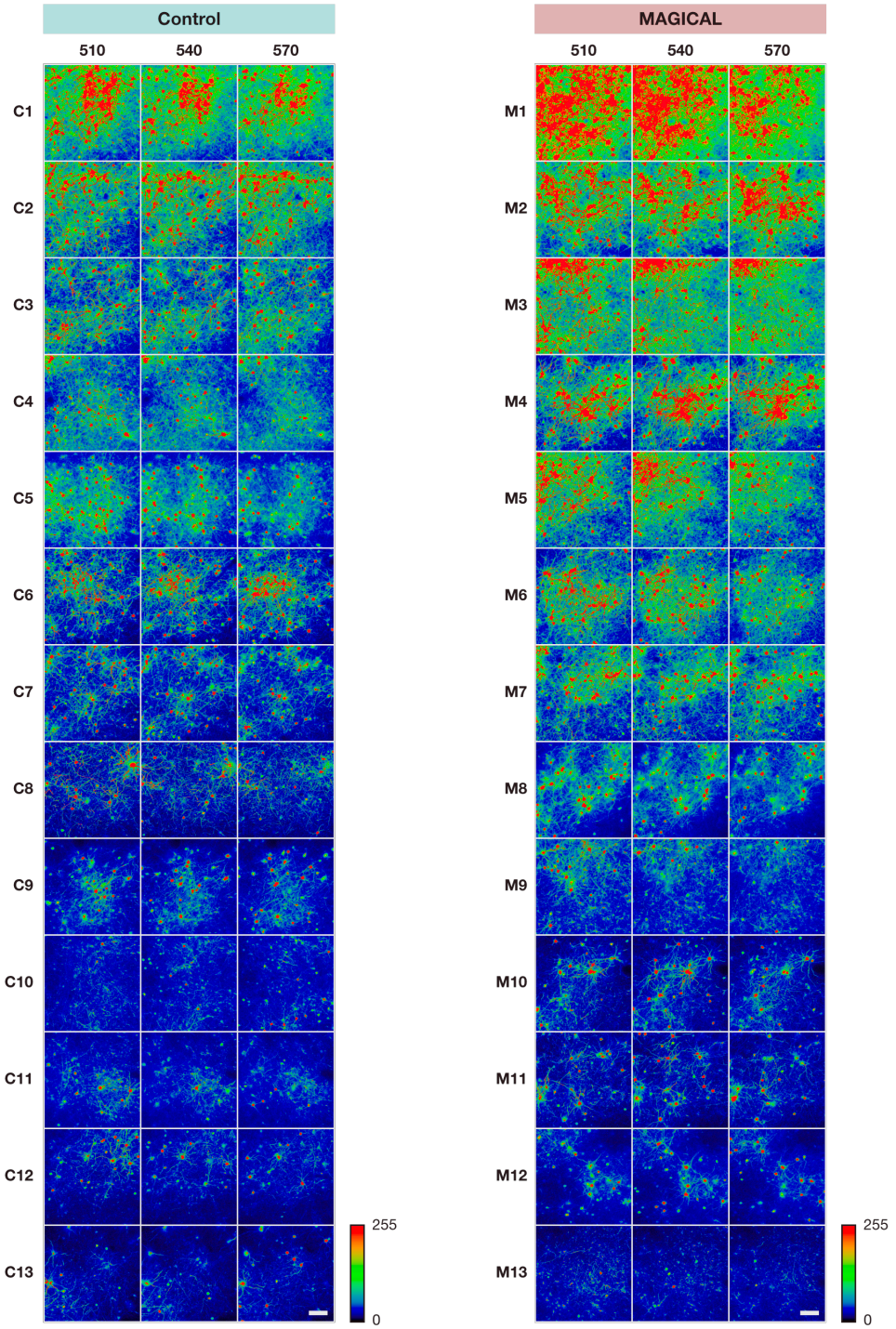

Figure S1. *In vivo* two-photon images at CxLV to evaluate fluorescence intensity. Related to Figure 1. All images were captured under the 25× Ob. with LP 66 mW and HV 30, as 3D stacks at indicated depth ± 3 μm with a 3-μm z-step size (3 sections). These 3D stacks were analyzed as FIDs (**Figure S2**) and FIPs for the GLMM (**Figure 1B–C**). All 3D stacks are displayed as MIP images, ranked by brightness scores (average fluorescence intensity per pixel) at 540 ± 12 μm depth (9 sections) captured with LP 66 mW and HV 30. scale bar 100 μm.

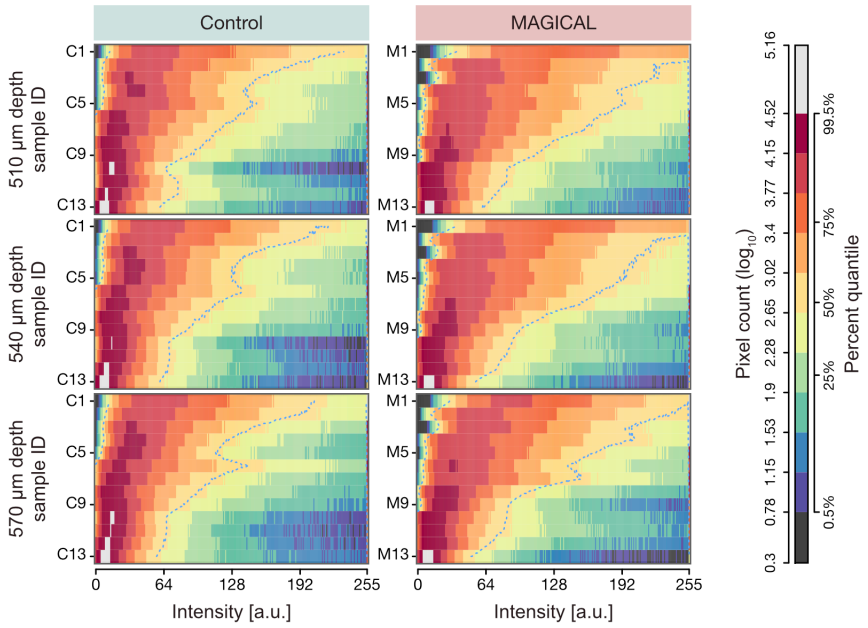

Figure S2. Heat map representation for FID of CxLV image stacks in Figure S1. Related to Figure 1. The heat map rows represent image stacks ranked by brightness scores at 540 ± 12 µm depth within each experimental group. The heat map columns represent intensity bins (8 bits). Pixel counts (z) in the FID histogram are converted with $\log_{10}(z+1)$ and assigned a color code. Pixel counts (excluding zero) were ranked in percent quantile. Cyan dotted contours are median. a.u., arbitrary unit.

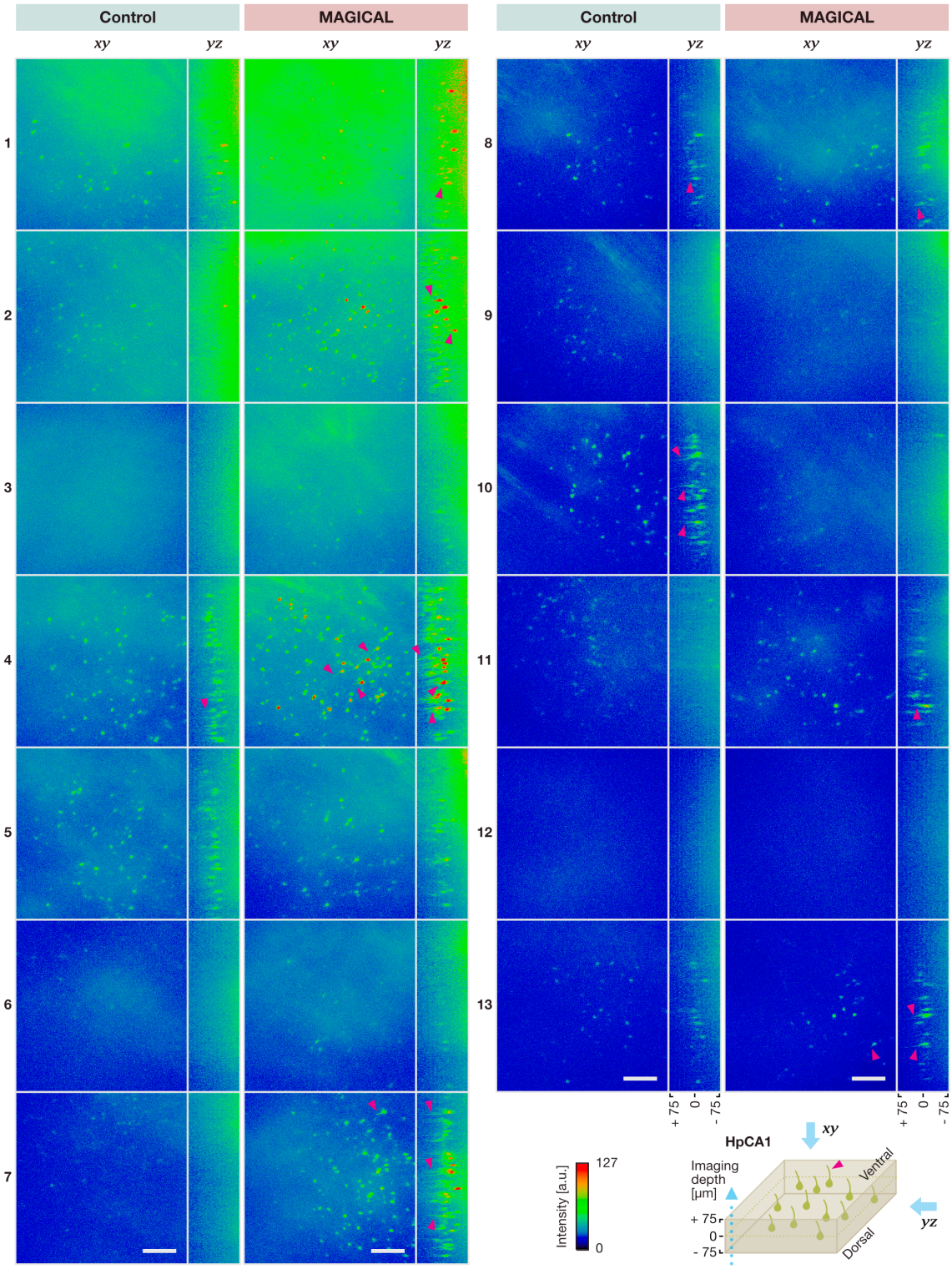

Figure S3. *In vivo* two-photon 3D rendering images at HpCA1. Related to Figure 2.
All images were captured under the 25× Ob. with LP 200 mW and HV 30, as 3D stacks at the middle of stratum pyramidale (0 μm relative depth) ± 75 μm with a 3-μm z-step size (51 sections). The 3D rendering was performed by using the Fiji's 3D project function with the brightest point mode and 50 % interior depth-cueing. Xy projection images were created from a ventral viewpoint (opposite side of observation), to avoid halation on the alveus (fibrous cloud structures) at the dorsal side. Yz projection images were created with rendering interpolation. These images are ranked by the brightness scores at 0 (center) ± 12 μm depth (9 sections). MAGICAL visualized many tiny apical dendrites (arrow-head) of pyramidal cells, although it is dependent on the signal to the background ratio. scale bar 100 μm. a.u., arbitrary unit.

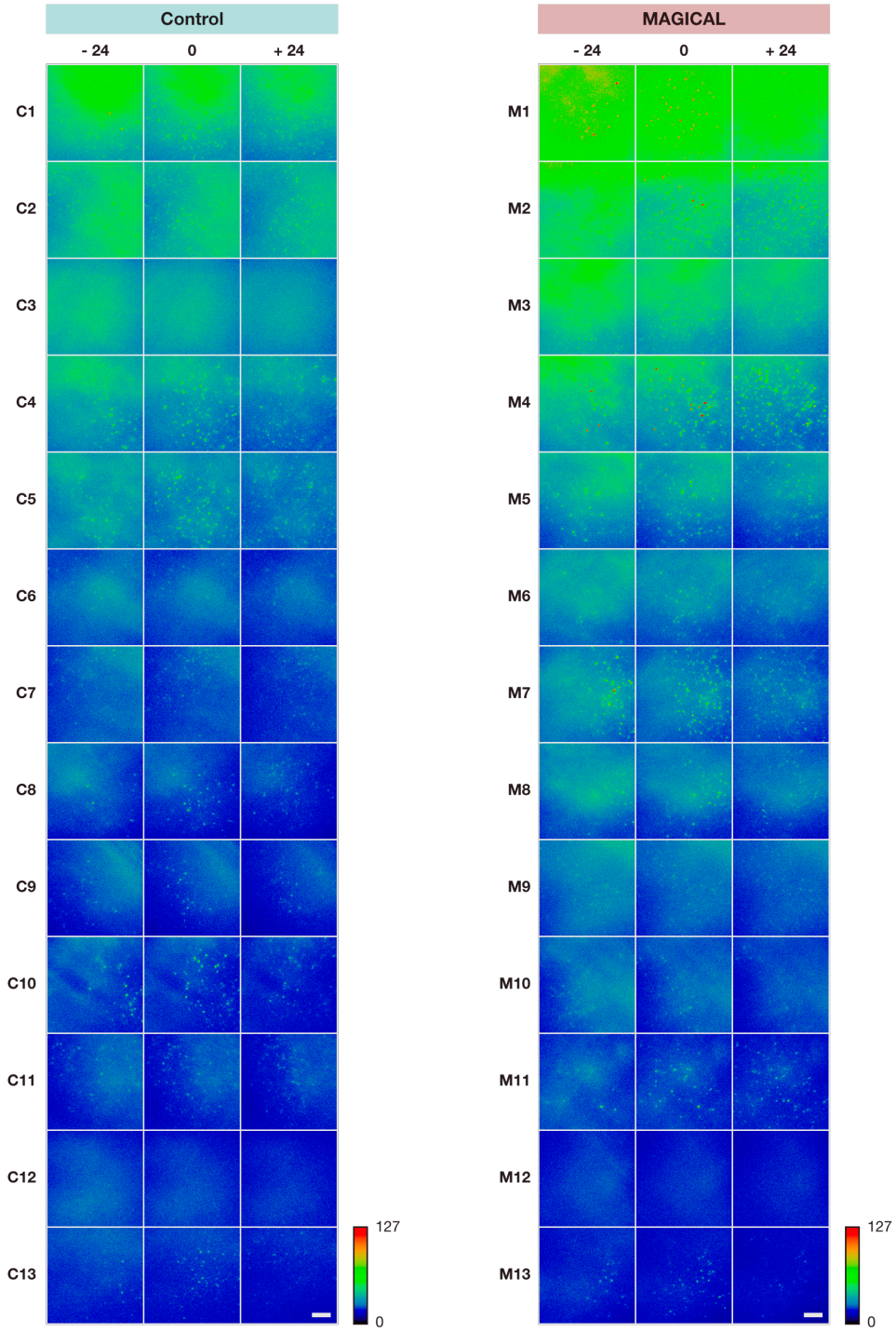

Figure S4. *In vivo* two-photon images at HpCA1 to evaluate fluorescence intensity. Related to Figure 2. All images were captured under the 25× Ob. with LP 200 mW and HV 30, as 3D stacks at indicated relative depth ± 3 μm with a 3-μm z-step size (3 sections). These 3D stacks were analyzed as FIDs (**Figure S5**) and FIPs for the GLMM (**Figure 2B–C**). All 3D stacks are displayed as MIP images, ranked by brightness scores at 0 (center) ± 12 μm depth (9 sections) captured with LP 200 mW and HV 30. scale bar 100 μm.

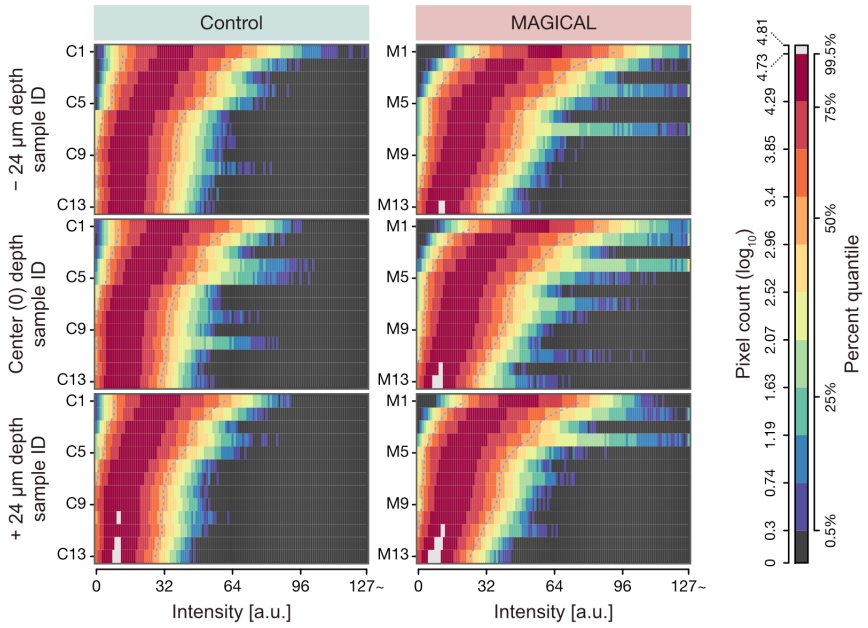

Figure S5. Heat map representation for FID of HpCA1 image stacks in Figure S4. Related to Figure 2. The heat map rows represent image stacks ranked by brightness at the center ± 12 µm depth within each experimental group. The heat map columns represent intensity bins (8 bits). Pixel counts (z) in the FID histogram are converted with $\log_{10}(z+1)$ and assigned a color code. Pixel counts (excluding zero) were ranked in percent quantile. Cyan dotted contours are median. a.u., arbitrary unit.

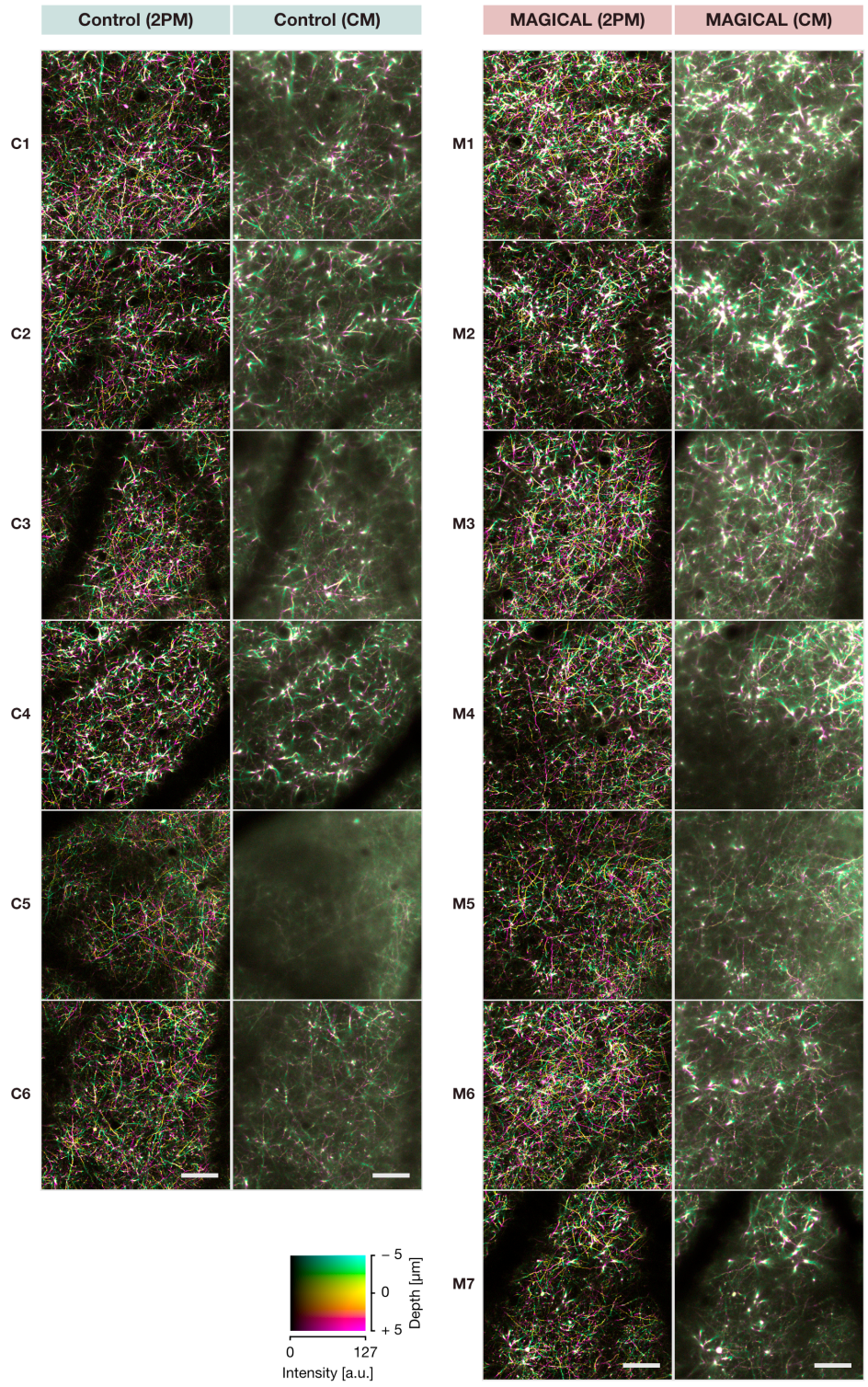

Figure S6. *In vivo* confocal images at CxLI. Related to Figure 3.
All images were captured as 3D stacks at 100 µm (center, 0 µm relative depth) ± 5 µm with a 1-µm z-step size (11 sections) under the 25× Ob., with LP 10 % and HV 90 in confocal microscopy and LP 16.1 mW and HV 30 in two-photon microscopy. All 3D stacks are displayed as DccMIP images, ranked by brightness scores in the confocal stacks. Intermediate images (C3 and M4) are shown as the representative images in **Figure 3A**. scale bar 100 µm. a.u., arbitrary unit.

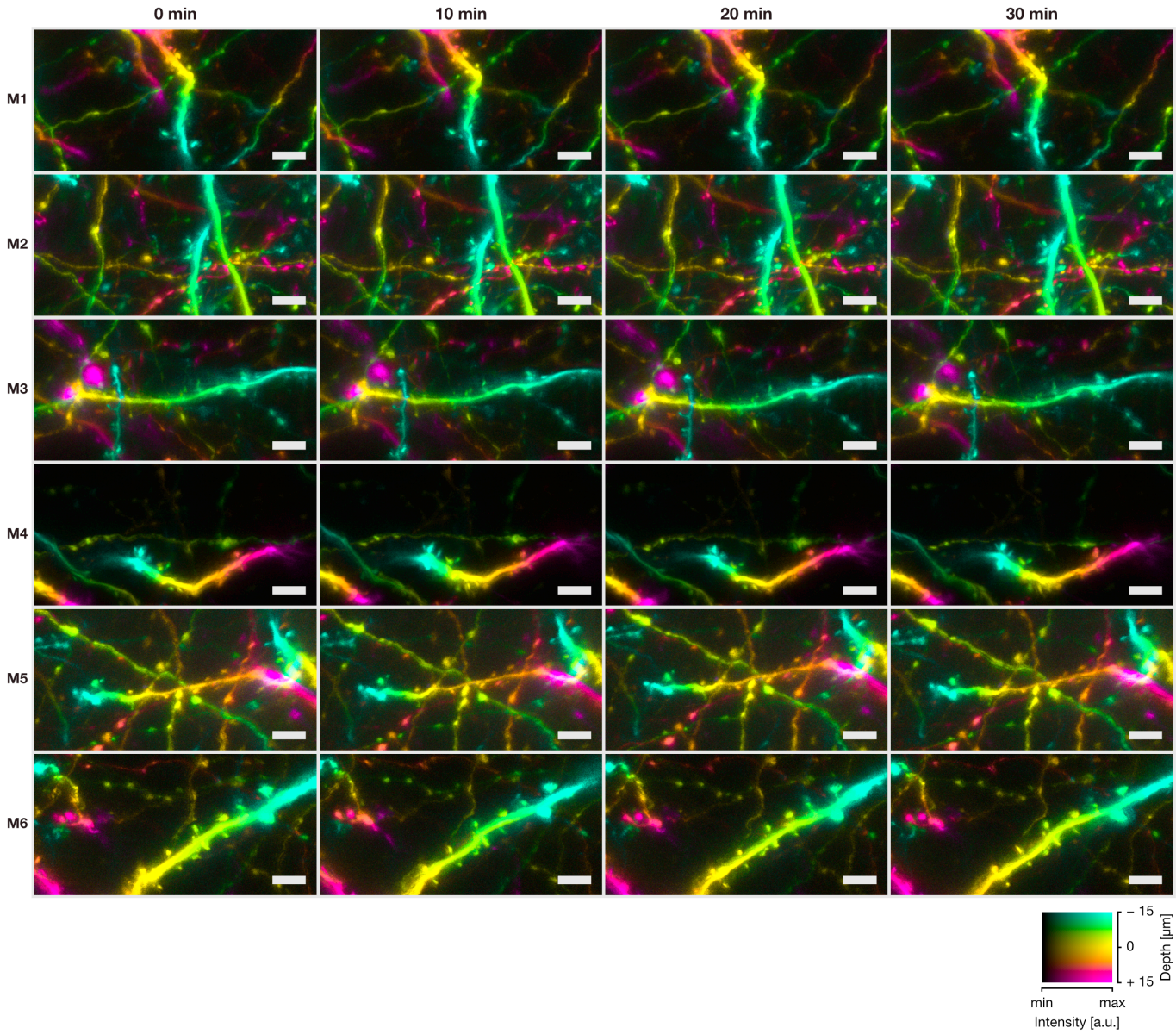

Figure S7. *In vivo* confocal high-resolution 4D images at CxLI. Related to Figure 4.
In 6 mice with MAGICAL, the 4D imaging was performed as 3D stacks with a 1-µm z-step size at approximate 100 ± 15 µm depth (31 sections, displayed as DccMIP), as a time-series at 5 minutes intervals for 30 minutes (7 time-points, but images at 5, 15, and 25 min were not shown). Laser power and detector sensitivity were set between 10 and 20 % and between HV 90 and HV 100, respectively. In the color code, each center depth is shown as 0 µm relative depth. The 3D images of M1 are shown in **Figure 4**. scale bar 5 µm. a.u., arbitrary unit.

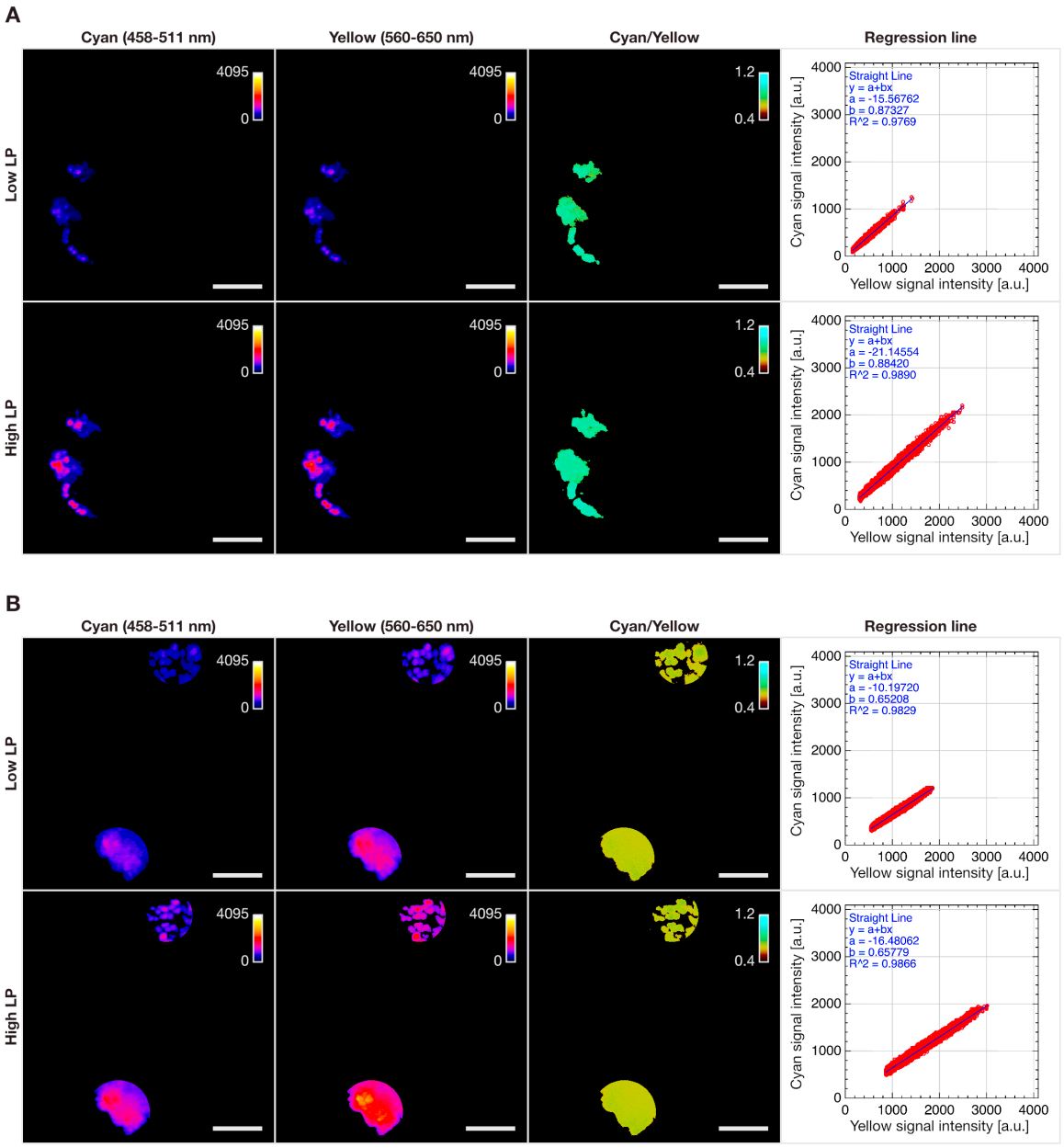

Figure S8. Cyan/Yellow ratio calculation for FESTA. Related to Figure 5.
(**A–B**) MIP images of beads clusters extracted via ROI, and respective regression lines at 100 μm (**A**) and 600 μm (**B**) depth. Although fluorescence intensity in each channel was affected by LP for two-photon excitation and the amount of fluorescence probe dependent on accumulation style of round-shaped beads, the Cyan/Yellow ratio was not affected. In contrast, the Cyan/Yellow ratio decreased with depth. scale bar 10 μm. a.u., arbitrary unit.

Table S1. The linear predictors in the GLMM. Related to Figure 1 and 2.

A

Fixed Effects :

Coefficient	Estimate	95 % CI lower	95 % CI upper	Std. Error	t value	Pr (> |z|)
(Intercept)	3.595	3.522	3.668	0.037	96.92	< 0.001
Depth_540	-0.024	-0.049	0.000	0.013	-1.92	0.0548
Depth_570	-0.044	-0.080	-0.009	0.018	-2.43	0.0153
Treatment_MAGICAL	0.259	0.164	0.355	0.049	5.33	< 0.001
Depth_540 : Treatment_MAGICAL	0.010	-0.024	0.044	0.017	0.57	0.5710
Depth_570 : Treatment_MAGICAL	-0.032	-0.080	0.016	0.024	-1.30	0.1928

Random Effects :

Group	Name	Variance	Std.Dev.
Mouse	(Intercept)	0.205	0.452
	Depth_540	0.002	0.050
	Depth_570	0.006	0.077
Residual		0.649	0.806

Number of observations: 929331, groups: Mouse, 26

B

Fixed Effects :

Coefficient	Estimate	95 % CI lower	95 % CI upper	Std. Error	t value	Pr (> |z|)
(Intercept)	3.044	2.973	3.115	0.036	84.31	< 0.001
Depth_000	-0.114	-0.122	-0.105	0.004	-27.01	< 0.001
Depth_+24	-0.230	-0.244	-0.217	0.007	-33.43	< 0.001
Treatment_MAGICAL	0.160	0.086	0.233	0.037	4.26	< 0.001
Depth_000 : Treatment_MAGICAL	-0.008	-0.020	0.004	0.006	-1.35	0.177
Depth_+24 : Treatment_MAGICAL	-0.011	-0.030	0.008	0.010	-1.15	0.250

Random Effects :

Group	Name	Variance	Std.Dev.
Mouse	(Intercept)	0.025	0.158
	Depth_000	0.000	0.008
	Depth_+24	0.000	0.013
Residual		0.159	0.398

Number of observations: 957264, groups: Mouse, 26

(**A–B**) Statistical results for the GLMMs with a Gamma error distribution and a log link function at CxLV (**A**) and HpCA1 (**B**). Wald-type 95 % CI was estimated for the coefficient of fixed effects by using the confint function.

Transparent Methods:

No statistical methods were used to predetermine sample sizes. In Generalized Linear Mixed Models (GLMMs), we used large sample sizes generally enough for modeling. For Welch's *t*-test, we confirmed that the *t*-test had adequate power, with a post-hoc test having effect size (Cohen's *d*), *p*-value (< 0.01), and the sample size.
The experiments were not randomized. *In vivo* imaging must observe individual mice convergently, not parallelly, for a long time. To reduce influence dependent on specific timing, the observation order for each experimental group should be uniformly mixed. However, the sample size is insufficient for randomization to ensure to equalize the order. Thus, we allocated mice to experimental groups so as not to localize the order.
Investigators were not blinded to allocation during experiments and data analysis. To remove observer bias during experiments, the observation area was selected by previously defined criteria, as described in "**Transparent** Methods, 'Fluorescence intensity analysis' section". Data collection and analysis were automatically performed by software with fixed parameter settings or macro programs.

Animals. All experiments were conducted in accordance with the Animal Research Committee of the Hokkaido University. The protocols were approved by the Committee on the Ethics of Animal Experiments in the Hokkaido University (No. 10-0119). Adult transgenic mice (9 to 12 weeks old, male) from Thy1-EYFP-H (H-line) were used for *in vivo* imaging of neurons. Adult C57BL/6NCr Slc mice (10 to 22 weeks old, male; Japan SLC, Shizuoka, Japan) were used for the FESTA with injected fluorescent beads. All mice were housed with food and drink *ad libitum* and were maintained in a 12 h light-dark cycle (lights on from 8:00 to 20:00), with controlled temperature (22 °C to 26 °C) and humidity (40 % to 60 %).

Glycerol administration. For MAGICAL mice, 5 % (w/v) glycerol (075-00616; Wako Pure Chemical Industries, Osaka, Japan) was administered orally in the drinking water, *ad libitum*, from 2 weeks prior to open-skull surgery to the end of the experiment, except during operations and observations. Control mice received only water.

Open-skull surgery. A cranial window was surgically created overlying the left cortex, according to a previous protocol (Holtmaat et al., 2009; Kawakami et al., 2013), with minor modifications. Briefly, 45 mg/kg-bw minocycline (Nichi-Iko Pharmaceutical, Toyama, Japan) were injected intraperitoneally (i.p.) about 4 h before surgery, to suppress bacterial infection and to protect neurons against microglial activation (neuroinflammation). Anesthesia was induced with an i.p. injection of 60 mg/kg-bw pentobarbital sodium (Somnopentyl; Kyoritsu Seiyaku Corporation, Tokyo, Japan), and was maintained with isoflurane inhalation (0.5 % to 1.5 %). To limit inflammation, 2 mg/kg-bw dexamethasone (Kyoritsu Seiyaku Corporation) was injected intramuscularly. Cranial bones were exposed, and then the left parietal bone was circularly carved about 4.2 mm in diameter with a dental drill and was removed gently. The exposed dura was washed with phosphate-buffered saline (PBS) to remove blood cells. A 4.2-mm diameter round coverslip (Micro Cover GLASS, #1S, about 0.17 mm thickness; Matsunami Glass Industry, Osaka, Japan), previously coated with a biocompatible polymer— Lipidure® (CM5206E; NOF Corporation, Tokyo, Japan), to prevent foreign-body reactions, especially to blood clotting— was placed directly over the dura without extra pressure, and was sealed on the bone edges with cyanoacrylate cement and dental adhesive resin cement (Super-Bond C&B; Sun Medical Company, Shiga, Japan). To make the foundations for chamber fixation, exposed cranial bones around the cranial window were partially coated with the adhesive resin cement. A head chamber, which has a center hole to expose the cranial window, was secured to the cranial bones with dental acrylic resin cement (Unifast III; GC Corporation, Tokyo, Japan). 5 mg/kg-bw carprofen (Rimadyl; Zoetis, Parsippany, NJ, USA) was injected i.p. to reduce inflammation and pain. After surgery, the mouse was singly housed for recovery for at least 3 hours until observation.

Beads injection. The beads injection into the cortex was performed in an open-skull surgery, with minor modifications before sealing with the coverslip, by using an oil-filled glass micropipette attached to a mechanically driven Hamilton microsyringe. The left parietal bone was elliptically resected about 3.9-mm in the anterior-posterior (A-P) axis and about 2.7-mm in the medial-lateral axis. A needle of the glass micropipette was inserted into the cortex at an angle of 54 degrees with respect to the brain surface, and proceeded 0.9 mm towards the anterior direction along the A-P axis, to reach about 0.72 mm depth. 1-μm YG beads (Fluoresbrite® YG Microspheres, Calibration Grade 1 μm, #18860; Polysciences, Incorporated, Warrington, PA, USA) were diluted at 4.6×10^8 beads/mL with PBS, and were gradually injected into the needle trace in repeated steps, in which the needle was withdrawn 0.3 mm and then was kept in place for 5 min. During and after the injection, the exposed dura was washed with PBS to remove blood cells and to prevent drying. After the surgery, the mouse was singly housed for recovery for at least one day until observation.

Setup of *in vivo* imaging. Between 3–12 hours or 1–2 days after surgery, *in vivo* fluorescence imaging was performed in H-line mice to observe neurons or in C57BL/6NCr Slc mice injected with artificial beads to do FESTA, respectively. All *in vivo* imaging sessions were conducted in mice anesthetized with isoflurane inhalation (Kawakami et al., 2013; 2015). The head chamber was mounted and glued to a customized adaptor stage, which suspended the mouse body with a harness, to reduce adverse effects due to movements. After setting under an upright microscope system, the adaptor stage was adjusted at a tilt angle, referring to 1-μm diameter fluorescent beads scattered on the coverslip as a guide, so that the cranial window was positioned horizontally, hence providing a suitable optical alignment. All *in vivo* imaging sessions were performed under a microscope system (A1R MP+ Multiphoton Confocal Microscope; Nikon, Tokyo, Japan) controlled by NIS-Elements software (version 4.13.00; Nikon) with 12-bit dynamic range. Before *in vivo* imaging, the z-position of the brain surface was set as zero for absolute depth.

Two-photon microscopy. *In vivo* two-photon imaging was performed with a water immersion objective (25× Ob., 1.10 NA) in PBS. The EYFP and the YG beads were excited by 960 nm and 900 nm, respectively, emitted from Ti:Sapphire laser (Mai Tai DeepSee; Newport Spectra-Physics, Irvine, CA, USA). By using a Galvano scanner in one-directional mode, the xy-images in the 3D stacks were acquired as 512 × 512 pixels at 1 frame per sec (fps), 2.2 μsec per pixel, which is the maximum speed in this condition. The 3D display was performed using the NIS-Elements software.

To visualize the neural circuits, all the EYFP signals under 650-nm wavelength were collected in a GaAsP type Non-Descanned Detector (GaAsP-NDD). The CxLV and HpCA1 images were captured as 3D stacks with a 3-μm z-step size. The depth of the CxLV was determined between 495 μm and 585 μm, where somas of CxLV pyramidal neurons were observed in every mouse. The depth of the HpCA1 was slightly different for each mouse, thus the middle of stratum pyramidale, approximately at 975 μm absolute depth, was set as the center depth of each HpCA1 stack. To evaluate the brightness of the images, laser power (LP) under the objective lens and detector sensitivity (HV: high voltage) were fixed. The CxLV was captured with LP 66 mW (under 25× Ob.) and HV 30. The HpCA1 was captured with LP 200 mW (under 25× Ob.) and HV 30.

For the FESTA, fluorescence signals were split into multi-colors by dichroic mirrors (DM) in front of the GaAsP-NDDs. The signals of YG beads were split by DM458, DM511, and DM560, and then separately detected at 458–511 nm (Cyan) and at 560–650 nm (Yellow). To avoid optical influence by injection trace, the FESTA applied to the beads clusters observable without crossing the trace. The beads images were captured as 3D stacks with a 0.25-μm z-step size at depth of interest ± 1.0 μm (9 sections). The detector sensitivities were fixed: HV 1 on the Cyan channel and HV 3 on the Yellow channel. The laser powers were adjusted for each bead cluster, because bead clusters show different brightness depending on cluster size and injection depth.

Confocal microscopy. *In vivo* confocal imaging was performed with a water immersion objective (25× Ob., 1.10 NA or 60× Ob., 1.20 NA) in PBS. The EYFP was excited by 488 nm, and its signal was collected at 500–550 nm in a standard detector. By using a Galvano scanner in one-directional mode, the xy-images comprising 3D stacks were acquired as 512 × 512 pixels at 1 fps or 512 × 256 pixels at 2 fps, 2.2 μsec per pixel, which is the maximum speed in this condition.

To evaluate observable depth in confocal imaging, the CxLI images were captured as 3D stacks with a 1-μm z-step size at 50 ± 5, 100 ± 5, and 150 ± 5 μm depth (11 sections) via a 25× Ob. Laser power and detector sensitivity were fixed at 10 % and HV 90, respectively. As references for confocal imaging, the same 3D stacks were also captured by using a two-photon microscope, of which detector sensitivity was fixed at HV 30, but 960-nm laser powers were adjusted to 12.5, 16.1, and 19.2 mW (under 25× Ob.) at 50, 100, and 150 μm depth, respectively.

High-resolution 4D imaging with a 60× Ob. was performed as 3D stacks with a 1-μm z-step size at approximate 100 ± 15 μm depth (31 sections), as a time-series at 5 minutes intervals for 30 minutes (7 time-points). Laser power and detector sensitivity were set between 10 and 20 % and between HV 90 and HV 100, respectively. The 3D display was performed by NIS-Elements software.

Fluorescence intensity analysis. For two-photon imaging at CxLV and HpCA1, 30 mice (Treatment: control, n = 15; MAGICAL, n = 15) were observed. For confocal imaging at CxLI, 17 mice (Treatment: control, n = 8; MAGICAL, n = 9) were observed. In the H-line mice, signal distribution is uneven, especially at the somatic layer, because the EYFP expression level varies among positive neurons, which tend to be differently clustered in different individuals. To avoid selection bias due to individual differences, the imaging area was selected according to the xy position where the hippocampus was observable at the most shallow depth.

Fluorescence intensity analysis was performed on the 3D image stacks, by using Fiji/ImageJ software (version 2.0.0-rc-49/1.51d) (Schindelin et al., 2012). For sorting of image stacks within each capture condition, mice were ranked in descending order of brightness (average fluorescence intensity per pixel) extracted from

image stacks around the center region: at 540 ± 12 μm for the CxLV, approximately at 975 ± 12 μm for the HpCA1, and at 100 ± 5 μm for the CxLI. The top or bottom brightness at each capture condition came from over- or under-exposed image stacks, respectively. Thus, mice having the top or bottom brightness within each treatment group were equally removed from the following analysis, as outliers of the capture condition. Finally, 26 mice (control, n = 13; MAGICAL, n = 13) and 13 mice (control, n = 6; MAGICAL, n = 7) were evaluated in fluorescence intensity analysis for two-photon imaging and confocal imaging, respectively. A representative image for each treatment group at each capture condition was obtained from the mouse scored as intermediate brightness.

In the two-photon imaging, we evaluated the fluorescence intensity distributions (FIDs) under HV 30, at three different depths within the observation area. For the CxLV, the three depths were set at 510 ± 3, 540 ± 3 (center), and 570 ± 3 μm depth. For the HpCA1, three depths were relatively adjusted at the middle of stratum pyramidale as the center (0 μm), approximately at 975 ± 3 μm absolute depth, and at 24 μm above and below the center. These three depths were sufficiently far away from each other to ensure separate images in the mice.

The FIDs were summarized to 8-bit intensity bins histograms by the Fiji and were visualized through the following steps by R (version 3.3.2) (R Core Team, 2016) with RStudio software (version 1.0.44). The histograms were arranged as a matrix, where the image stacks were sorted in rows according to their brightness in decreasing order, and the intensity bins were aligned in columns. Pixel counts (z) in the histogram were converted with $\log_{10}(z+1)$, where 1 is a constant to avoid $\log_{10}(0)$ contamination in the converted matrix. The matrix of FIDs was visualized as a heat map. Pixel counts (excluding zero) were ranked in percent quantile. In the heat maps, the 50 % quantile was shown as cyan dotted contours.

Image similarity analysis. Based on image features, similarities between CM images and 2PM reference images at the same CxLI areas were evaluated in 13 mice (Treatment: control, n = 6; MAGICAL, n = 7), which passed fluorescence intensity analysis to remove outliers. The 3D stack images were converted to DccMIP 2D images with a color code shown in **Figure 3A**, by using Fiji/ImageJ software. The display ranges of fluorescence intensity (min–max in 8 bits) were adjusted as follows: 2PM images at every depth, (0–127); CM images at 50, 100, and 150 μm depth, (0–255), (0–127), and (0–63), respectively.

Features extraction and comparison were performed by using OpenCV (version 3.4.2) via a python (version 3.6.6) code. In gray-scale space, a Histogram of Oriented Gradients (HOG) (Dalal and Triggs, 2005) feature was extracted from each image (512 × 512 pixels) with parameters as follows: window size, (512, 512); block size, (128, 128); block stride, (4, 4); cell size, (16, 16); nbins, 180; other parameters were used as preset in OpenCV. The raw HOG feature comprising 108,391,680 bins was normalized to 1 to convert a probability histogram. In the comparison between the paired two images, a similarity index was defined as the intersection probability of the HOG features.

Fluorescence Emission Spectrum Transmissive Analysis. For spectral ratio calculation, data processing was performed by using the Fiji/ImageJ software (version 2.0.0-rc-49/1.51d) (Schindelin et al., 2012). All xy images in raw data (multi-color 3D stack) were smoothed with the median filter (1 pixel). Pixels having faint or saturated signal values (< 32 or 4063 < in 12 bit, respectively) were excluded from the following calculation. Background area out of beads was detected by an auto-threshold function with the Otsu method on the Yellow channel and was removed from all channels. Spread bead cluster images were selected by ROI (region of interest) to exclude the injection trace from the calculation. The pixels in YG bead clusters were plotted on a scatter graph, corresponding to the Yellow intensity along the x-axis and the Cyan intensity along the y-axis. At depth of interest, a representative Cyan/Yellow ratio was determined from the slope of the best-fitted regression line (highest R^2) on the scatter plot, derived from image stacks at its depth ± 1.0 μm. To calculate the ∆Cyan/Yellow, the Cyan/Yellow ratio was divided by the average of Cyan/Yellow within the experimental group at 100 μm depth.

Statistics. All statistical analysis was performed by using R (version 3.3.2) (R Core Team, 2016) with RStudio software (version 1.0.44). Conventional two-tailed Welch's t-test and Cohen's d were calculated with the default and the MBESS package (version 4.3.0), respectively. Permuted Brunner-Munzel (Brunner and Munzel, 2000; Neubert and Brunner, 2007; Neuhäuser and Ruxton, 2009) test was executed by the lawstat package (version 3.1) with permutation code.

To assess MAGICAL effects on FIDs, we constructed GLMMs with a Gamma error distribution and a log link function. In the models, fluorescence intensities of pixels (FIPs) were used as a response variable. The FID of each image stack at the depth ± 3 μm, therefore, was re-expanded to an intensity list comprised of 786,432 pixels (512 × 512 pixels × 3 sections). To reduce modeling costs, 12,288 pixels (1.56 %) were randomly sampled without overlap from each list. Saturated pixels (255 in 8 bit) were excluded from modeling due to inaccuracies in fluorescence intensity. Zero intensity pixels were also excluded to avoid a calculation failure under the log-link

function. “Treatment” (2 levels, MAGICAL or control) and “Depth” (3 levels) were used as categorical predictor variables with fixed effects. The models included an interaction between “Treatment” and “Depth.” To overcome pseudo-replications caused by sampling multiple pixels within each mouse, “Mouse” (26 mice in total) was assigned as a random effect for intercepts and “Depth” slopes. Thus, the models were described in R as follows:
FIP ~ Depth * Treatment + (Depth | Mouse)
Consequently, the models comprised 929,331 (CxLV) or 957,264 (HpCA1) pixel observations, in 78 image stacks extracted at 3 depths from 26 mice under 2 treatments.

The model fitting was performed via the maximum likelihood according to Laplace approximation, by using the glmer function in the lme4 package (version 1.1-12). For the estimated coefficient of fixed effect, Wald-type 95 % confidence interval (CI) was calculated by using the confint function. The model prediction for each image stack was obtained through the predict.merMod function in the lme4 package. The fixed effects with asymptotic 95% CI were estimated by using the Effect function in the effects package (version 3.1-2). Pairwise comparisons for the predictor variables were examined by the lsmeans function in the lsmeans package (version 2.25-5).

As the coefficient of determination for the GLMM, two R^2 statistics are proposed (Nakagawa and Schielzeth, 2013): marginal and conditional R^2_{GLMM}. The marginal R^2_{GLMM} ($R^2_{GLMM(m)}$) describes the proportion of variance explained only by fixed effects. The conditional R^2_{GLMM} ($R^2_{GLMM(c)}$) describes the proportion of variance explained by both fixed and random effects.

$$R^2_{GLMM(m)} = \frac{\sigma^2_{fix}}{\sigma^2_{fix} + \sigma^2_{random} + \sigma^2_{residual}} \quad (1)$$

$$R^2_{GLMM(c)} = \frac{\sigma^2_{fix} + \sigma^2_{random}}{\sigma^2_{fix} + \sigma^2_{random} + \sigma^2_{residual}} \quad (2)$$

An original method for the R^2_{GLMM} was limited only to the GLMM including Poisson or binomial error distributions and not including random slope terms (Nakagawa and Schielzeth, 2013). However, two extensions had been individually provided for the R^2_{GLMM}, to calculate random effects variances in random slope models (Johnson, 2014) or to evaluate further error distribution in the residual variance (Nakagawa and Schielzeth, 2016). Thus, we calculated the R^2_{GLMM} of our models by an R code combining the two extensions as follows: in the extension for random slope models (Johnson, 2014), a provided code generates a square matrix at once but uses only diagonal elements of the matrix. When the code ran for our models, a large number of observations generated a huge square matrix, which caused the computation to fail, due to insufficient memory. Therefore, we calculated only the portion corresponding to the diagonal of the square matrix. On the other hand, the extension for residual variances was applicable to our models without modifications. We selected the trigamma function from three candidates in the paper (Nakagawa and Schielzeth, 2016), to evaluate the models including a Gamma error distribution and a log link function.

Supplemental References:

Brunner, E., and Munzel, U. (2000). The nonparametric Behrens‐Fisher problem: asymptotic theory and a small‐sample approximation. Biom. J. *42*, 17–25.

Dalal, N., and Triggs, B. (2005). Histograms of oriented gradients for human detection. 2005 IEEE Comput. Soc. Conf. Comput. Vis. Pattern Recognit. (CVPR'05) *1*, 886–893.

Johnson, P.C.D. (2014). Extension of Nakagawa & Schielzeth's R^2_{GLMM} to random slopes models. Methods Ecol. Evol. *5*, 944–946.

Nakagawa, S., and Schielzeth, H. (2013). A general and simple method for obtaining R^2 from generalized linear mixed‐effects models. Methods Ecol. Evol. *4*, 133–142.

Nakagawa, S., and Schielzeth, H. (2016). Coefficient of determination R^2 and intra-class correlation coefficient ICC from generalized linear mixed-effects models revisited and expanded. bioRxiv 095851.

Neubert, K., and Brunner, E. (2007). A studentized permutation test for the non-parametric Behrens–Fisher problem. Comput. Stat. Data Anal. *51*, 5192–5204.

Neuhäuser, M., and Ruxton, G.D. (2009). Distribution-free two-sample comparisons in the case of heterogeneous variances. Behav Ecol Sociobiol *63*, 617–623.

R Core Team (2016). R: a language and environment for statistical computing.

Schindelin, J., Arganda-Carreras, I., Frise, E., Kaynig, V., Longair, M., Pietzsch, T., Preibisch, S., Rueden, C., Saalfeld, S., Schmid, B., et al. (2012). Fiji: an open-source platform for biological-image analysis. Nat Methods *9*, 676–682.